Journal of Geophysical Research: Solid Earth

RESEARCH ARTICLE
10.1029/2017JB015238

Multiple Phase Changes in the Mantle Transition Zone Beneath Northeast Asia: Constraints From Teleseismic Reflected and Converted Body Waves

Benoit Tauzin[1,2], **Seongryong Kim**[3], **and Juan Carlos Afonso**[4,5]

[1]Université de Lyon, UCBL, ENSL, CNRS, LGL-TPE, Villeurbanne, France, [2]Research School of Earth Sciences, Australian National University, Canberra, ACT, Australia, [3]School of Earth and Environmental Sciences, Seoul, South Korea, [4]Department of Earth and Planetary Sciences, Macquarie University, Sydney, New South Wales, Australia, [5]Centre of Earth Evolution and Dynamics, Department of Geosciences, University of Oslo, Oslo, Norway

Key Points:
- We investigate Northeast Asia mantle transition zone structure from receiver functions and SS precursors
- We find complex layering with multiple seismic discontinuities at the tip of the subducted Pacific plate
- Thermodynamical modeling suggests temperatures of 1000–1300 K and transitions in the olivine and garnet systems

Supporting Information:
- Supporting Information S1
- Text S1
- Text S2

Correspondence to:
B. Tauzin,
benoit.tauzin@univ-lyon1.fr

Citation:
Tauzin, B., Kim, S., & Afonso, J. C. (2018). Multiple phase changes in the mantle transition zone beneath northeast Asia: Constraints from teleseismic reflected and converted body waves. *Journal of Geophysical Research: Solid Earth*, *123*, 6636–6657. https://doi.org/10.1029/2017JB015238

Received 16 NOV 2017
Accepted 9 JUN 2018
Accepted article online 15 JUN 2018
Published online 11 AUG 2018

Abstract We reassess the mantle transition zone structure below the northeast Asia margin in the context of subduction of the Pacific plate below the Eurasian continent. We use two independent approaches of teleseismic imaging, namely, compressional-to-shear converted waves (receiver functions) and shear wave underside reflections (SS precursors), and compare them within their statistical uncertainties. We find localized complexity in the interfaces marking solid phase changes in mantle minerals, in terms of both apparent topography and reflectivity. The 660-km discontinuity is doubled, with ~80-km maximum vertical distance between the interfaces, over an 890 × 350 km^2 region between 36–44°N and 130–133°E at the tip of the subducted Pacific plate. A similar complexity exists on the 410-km discontinuity, coinciding with the presence of a deep cluster of seismicity below the Japan Sea. Both methods suggest the presence of low-velocity zones atop the 410, within the mantle transition zone, and below the 660. This complex seismic signature is related to the Pacific plate and interpreted in light of the subduction thermal regime and phase equilibria for a pyrolitic mantle composition. Phase changes manifest themselves as broad zones of velocity gradients with localized doubled or multiple first-order discontinuities, associated with transitions in the olivine, pyroxene, and garnet systems. An average pyrolitic composition and local temperatures of 1000–1300 K can explain the observed velocity gradients and multiple discontinuities. We show that the dissolution of stishovite, a high-pressure polymorph of SiO_2, into the higher-pressure perovskite mineral, is a possible explanation for the low-velocity zones at the top of the lower mantle.

Plain Language Summary In the early 1990s, the idea emerged that the study of seismic discontinuities near 410- and 660-km depths could inform us about the vertical circulation of material in the mantle. These two discontinuities were assigned to solid phase changes of a silicate mineral rich in magnesium (90%) and iron (10%), olivine. Advances in the field of mineralogy and high-pressure physics suggested, however, that other minerals, garnet and pyroxenes, should contribute to the general seismic signature. Due to the limited imaging capability of seismological methods and station deployments, however, a one-to-one correspondence between observed seismic structure and mineralogy has remained elusive, at best controversial. We provide here from two independent approaches compelling evidence for localized complexity in the seismic structure near 410- and 660-km depths, which we relate, through mineralogical modeling, to phase changes in olivine, garnet, pyroxene, and silica systems. This work provides the observational basis for assessing the viability of geodynamic and thermochemical models of the mantle beneath the northeast Asia margin.

1. Introduction

The mantle transition zone (MTZ) is an ~250-km-thick boundary layer delimited by two seismic interfaces, the so-called 410- and 660-km discontinuities, which are attributed to solid-solid phase changes from olivine (ol) to wadsleyite (wa) and ringwodite (rw) to perovskite+magnesiowustite (ppv+mw; Bina & Helffrich, 1994). An enigmatic patchwork of low-seismic velocity zones (LVZs) was reported at various scales and depths within

or surrounding the MTZ (e.g., Shen et al., 2014; Tauzin et al., 2010, Tauzin, Kim, & Kennett, 2017; Vinnik & Farra, 2007). These LVZs might be distinctive features of a well-mixed convective mantle that preserves small-scale compositional heterogeneities. They are usually attributed to the volatile content (H_2O, CO_2; Bercovici & Karato, 2003; Hier-Majumder & Tauzin, 2017) or to remnants of subducted oceanic crust in the MTZ (Shen & Blum, 2003; Shen et al., 2014). High-resolution mapping of these LVZs at regional scale is thus crucial for our understanding of the recycling of geochemical heterogeneities within large-scale limbs of thermally driven mantle convection (Tauzin, Kim, & Kennett et al., 2017; Wei & Shearer, 2017).

In addition to the polymorph transitions in olivine, other mineral phases such as pyroxenes and garnet also experience solid-solid transformations that increase the complexity of the elastic gradients observed within and around the MTZ (Vacher et al., 1998; Weidner & Wang, 1998). Such a spatial complexity has been found near a deep cluster of seismicity at the base of the MTZ beneath northeast China, at the tip of the deeply subducting Pacific plate. The 660-km boundary in this region is ~30–50 km deeper than the global average of ~660 km (Liu et al., 2015). Multiple velocity jumps have been also reported between 650- and 750-km depths, 200–300 km north of this depression (Ai & Zheng, 2003; Niu & Kawakatsu, 1996). This complexity has been attributed to multiple phase changes in the garnet-pyroxene component, from garnet-to-ilmenite, and ilmenite-to-perovskite (Ai & Zheng, 2003). Such phase changes could also occur in the coldest regions of the MTZ below western United States and Europe, as suggested by Simmons and Gurrola (2000), Tauzin and Ricard (2014), Bonatto et al. (2015), and Cottaar and Deuss (2016). A close examination of the spatial complexity of the MTZ may therefore provide a clue on the chemical and thermal conditions prevailing in the formation of the LVZs.

Seismic tomography delineates smooth changes in wave speed associated with mantle convection, but one must focus on the scattered wavefield to image interfaces and layers associated with transitions in mineral assemblages. Stacking of teleseismic data from dense source and receiver arrays allows to produce images of the MTZ by enhancing weak signals from scattered waves (Shearer, 1991). Scattering as precursors of the SS phase (SdS; Figure 1b), first recognized in the early 1990s (Shearer, 1991), has been used to constrain the long-wavelength MTZ structure (e.g., Flanagan & Shearer, 1998; Gu et al., 1998). However, the most detailed constraints have come from compressional waves converted into shear waves (Pds; Figure 1a) and the processing of data from dense arrays of seismometers at continental scale (see, e.g., Niu et al., 2005; Schmandt et al., 2012; Tauzin et al., 2013).

Both approaches have advantages and drawbacks and can be considered complementary. SdS sample the MTZ discontinuities near the bounce point, halfway between sources and receivers (Figure 1b). They provide good global coverage, but they are analyzed at long period (in general, larger than 15 s), which limits their lateral resolution to ~1,000 km (Shearer, 1991). Here we analyze this data at shorter period, 10 s, enhancing the resolution to about 800 km. Pds phases provide a better lateral resolution (150–200 km) beneath the stations, but the coverage is limited by the geographical distribution of seismometers (Figures 1a, 1c, and 1d), with major gaps in oceanic areas. In comparison with earlier studies of the northeast Asia margin (e.g., Lee et al., 2014; Li et al., 2000; Liu et al., 2015; Niu et al., 2005), we improve the coverage by combining data from permanent and temporary seismic networks across the Japanese Islands, the Korean peninsula, and northeast China (Figures 1c and 1d; Tauzin, Kim, & Kennett, 2017).

A debate exists on the consistency of the estimates of the MTZ structure based on Pds and SdS data (e.g., Chevrot et al., 1999; Lawrence & Shearer, 2006). Theoretically, the large size of the Fresnel zone for SdS is expected to prevent the use of geometrical optics (ray theory) to relate arrival times to discontinuity depth at the bounce point (Chaljub & Tarantola, 1997; Dahlen, 2005; Koroni & Trampert, 2015; Zhao & Chevrot, 2003). In this way, Chaljub and Tarantola (1997) showed with finite difference numerical experiments that small-scale (~500 km) lateral variations in the topography of boundaries may be observed on individual waveforms over larger distances, exceeding 1,000 km in surface. Chevrot et al. (1999) and Zhao and Chevrot (2003) attribute the absence of correlation between differential traveltimes of waves converted and reflected at MTZ boundaries to this phenomenon. In contrast, Shearer et al. (1999) showed from migration experiments that the mapping from SdS data does not result in a significant *leakage* of the small-scale structure into the larger-scale structure. Lawrence and Shearer (2006) also showed that the observed global range of variations in the MTZ structure from both SdS and Pds studies is in agreement when accounting for the smoothing effect of the larger SdS Fresnel zone. Schmerr et al. (2013) performed synthetic tests and found that only interfaces that exist over horizontal distances larger than 500 km were likely to be accurately resolved by SdS. A tomographic

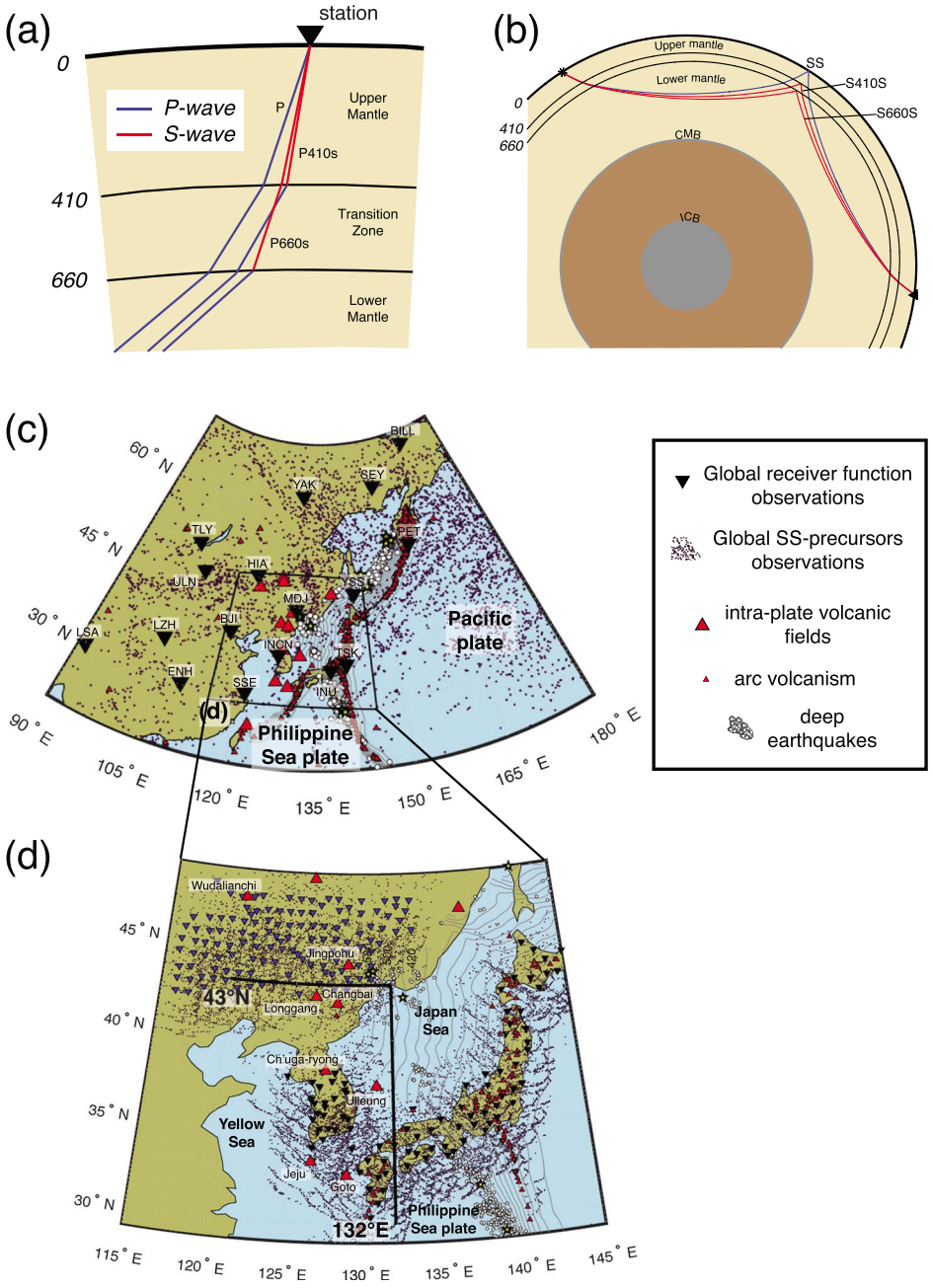

Figure 1. Global and regional data sets of teleseismic body waves converted and reflected at seismic boundaries of the mantle transition zone. (a) Ray geometry for the *P*, P410s, and P660s converted phases (receiver functions) recorded at three-component broadband stations. (b) Ray geometry for the SS, S410S, and S660S underside reflections (SS precursors) halfway between seismic sources and receivers. (c) Map of the geographical distribution of the 5027 SS precursors reflection points (black dots) and of observations at permanent stations from the global study of Tauzin et al. (2008) (black triangles). The depth contours of the subducted Pacific and Philippine plate (Hayes et al., 2012) are marked with gray lines. Small red triangles locate arc-related volcanoes. Large red triangles designate intraplate volcanic fields. White dots locate deep focus subduction zone earthquakes within the transition zone from the U.S. Geological Survey (USGS) catalog, black stars represent events with magnitude larger than 7.0. The black frame corresponds to the zone enlarged in (d). (d) The 232 stations used in our regional receiver function analysis (inverted triangles) with the coverage in *P*-to-*S* conversion points at the 660-km depth discontinuity (black dots). We use the F-Net broadband seismic network in Japan (black triangles), the permanent seismic network in Korea (black triangles), and the portable seismic experiment NECESSArray in northeast China (blue triangles). Two profiles along which the seismic image is obtained in Figure 4 are located at 43°N and 132°E.

model of the northeast Asia margin, obtained from nonlinear waveform inversion of stacked SdS waveforms, showed also good agreement with models obtained from classical body wave traveltime tomography (Dokht et al., 2016; Obayashi et al., 2013).

Here we perform, for the first time in a regional study, a systematic comparison of passive imaging of the MTZ using both teleseismic scattered SdS and Pds wavefields. We use a high-quality subsample (5,027 waveforms) of a global database of 15,432 intermediate-period (10 s) records of the SdS phases for our large-scale imaging. SdS measurements are compared with large-scale long-period (10 s) Pds observations at 16 seismic stations from a global database (Tauzin et al., 2008). They are also compared with high-resolution observations from 41,814 shorter-period (5–75 s) Pds waveforms (receiver functions [RFs]), recorded at 232 broadband seismic stations (Tauzin, Kim, & Kennett, 2017).

This paper provides the observational basis for interpretations of seismic signals in terms of mineralogy and phase stability of deep mantle assemblages as well as for assessing the viability of geodynamic and/or thermochemical models of the mantle beneath the study region. In subsequent work, we will use numerical modeling to investigate in more detail possible thermochemical structures required to explain the seismic observations. Ultimately, we aim at jointly fitting the portions of the waveforms associated with the fine structure of the discontinuities near the 410- and 660-km phase changes, and the MTZ thickness, without correcting for the volumetric velocity heterogeneities. The underlying assumption is that MTZ seismic observables can be self-consistently predicted from physical Earth's models (i.e., temperature and composition). This paper also highlights the issue of sensitivity of both Pds and SdS data types. Compared to our previous RF study (Tauzin, Kim, & Kennett, 2017), we focus here on the seismic signature of the 410- and 660-km phase changes and also investigate whether the pervasive low-velocity zones identified from regional Pds data can be identified using SdS data.

2. Data and Methods

2.1. Receiver Functions (Pds RFs)

The Pds observations at the 16 stations in Figure 1c come from a global database of observations of the MTZ discontinuities at 167 stations, from eight global and regional permanent networks. The detail of the processing for extracting the *P*-to-*S* converted wavefield is described by Tauzin et al. (2008). It includes rotation of the recording components along the *P* and SV directions of vibration, filtering at long period (> 10 s), and the construction of RFs (Ammon, 1991) through iterative time domain deconvolution (Ligorrìa & Ammon, 1999). The RF data are then slant stacked, with the extraction by stations of a single time domain average RF for a reference epicentral distance of 65°. The differential traveltimes between the direct *P* wave and P410s and P660s phases are measured with bootstrap resampling and converted to depth using the *iasp91* velocity model (Kennett & Engdahl, 1991).

At regional scale (Figure 1d), we use the waveforms of 531 teleseismic earthquakes recorded at 232 three-component broadband seismic stations from dense arrays located on the Korean peninsula, in Japan (F-Net), and in northeast China (NECESSArray) (Tauzin, Kim, & Kennett, 2017). The earthquakes have magnitude ranging between 5.5 and 7.2 and were recorded at epicentral distances between 40° and 90°. We refer to Tauzin, Kim, & Kennett (2017) for details on the processing. A difference with our global study (Tauzin et al., 2008) is that, before deconvolution, the records are rotated along the radial and vertical directions and low-pass filtered with a higher-corner frequency, 0.2 Hz. The final regional RF data set is composed of 41,814 waveforms and provides a good coverage in *P*-to-*S* piercing points across the 410- and 660-km discontinuities below the arrays (Figure 1d).

Resulting RFs are shown in Figure 2b, partially stacked in bins of 1° epicentral distance, and compared with the result of modeling synthetic RFs with the iasp91 velocity structure in Figure 2d (Kennett & Engdahl, 1991). We created full-waveform synthetic seismograms for the exact source-receiver pairs observed in our database using the reflectivity algorithm from Fuchs and Muller (1971). We used source parameters from the global CMT catalog (http://www.globalcmt.org/) and processed the synthetic seismograms the same way as the real data. On both sections, we observe the conversion at the Moho discontinuity Pms, the crustal multiples PPms and PSms, and the conversions at MTZ boundaries P410s and P660s. In the observed seismic section and stack of the whole set of data (Figure 2b), a faint positive arrival is observed between the P410s and P660s phases which could correspond to a conversion at the weak 520-km discontinuity (Shearer, 1996).

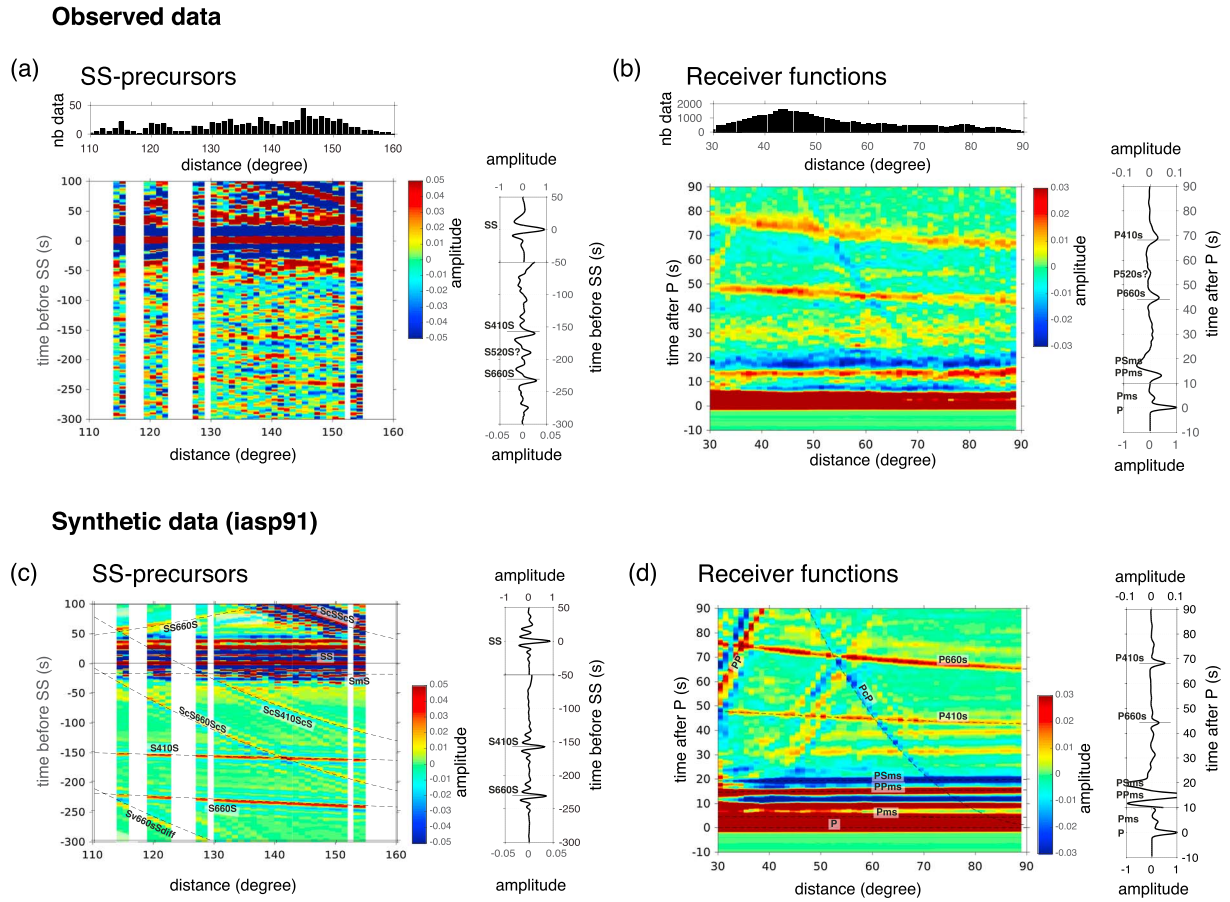

Figure 2. Waveforms of teleseismic converted and reflected body waves. Observed (a) SS precursors and (b) receiver function waveforms. The full data sets in the region shown in Figure 1d are partially stacked in bins of 1° epicentral distance. The stack of all the data is shown after moveout correction in the panels at right. The amplitude of reflected/converted waveforms is scaled relative to the mother phase (SS or *P*). The distribution of the data as a function of epicentral distance is shown in the histograms on top. (c, d) Same as (a) and (b) except that we present synthetic seismic sections computed from the iasp91 velocity structure (Kennett & Engdahl, 1991). Major seismic phases are labelled with, superimposed (dashed lines), the traveltime curves predicted by the iasp91 velocity model.

RFs such as those shown in Figures 2b and 2d, with variable incidence angles and back azimuths, are combined using a common conversion point (CCP) stacking procedure (Wittlinger et al., 2004) to form 2-D images of the seismic reflectivity structure (Figures 3b, 4b, 5a, and 6d, 6g). The approach follows the steps described by Tauzin et al. (2013), Hier-Majumder and Tauzin (2017) and Tauzin, Kim, & Kennett (2017), with ray tracing in a one-dimensional Earth's model, conversion of the RFs from the time domain to the depth domain, and their projection and stacking onto the vertical plane of the profiles. Our emphasis in this paper is on comparing the results between the Pds and SdS methods, and image intermittent and/or fine-scale structure on discontinuities, rather than obtain the most accurate discontinuity depth estimates. We therefore use the iasp91 velocity model (Kennett & Engdahl, 1991) for ray tracing and back projection.

The result of such an imaging, using the synthetic data computed in the iasp91 structure and along two profiles at 132°E and 43°N, is shown in Figure 3b. The Moho discontinuity is located at 35-km depth. The sequence of alternating amplitudes between 100 and 200 km depths is associated with the PPS and PSS crustal reverberations, above the Conrad and Moho discontinuities. These crustal multiples prevent us from interpreting the structure within this depth range. Deeper, the only visible interfaces are the 410- and 660-km discontinuities with amplitudes of 0.9–1.4% and 1.6–2.7% the *P* wave, respectively. As previously discussed by Tauzin, Kim, & Kennett (2017), faint negative signals (> −0.5% the *P* wave amplitude) are also distributed at the base of the MTZ, resulting from sidelobes and phase interference effects.

For the observed CCP-stacked data, we show in Figure 3d two standard deviations on the stacked amplitudes (Efron & Tibshirani, 1991; Press et al., 1992; Tauzin, Kim, & Kennett, 2017). These two standard deviations represent the 95% confidence level on stacked amplitudes and are regarded as a measure of the noise level.

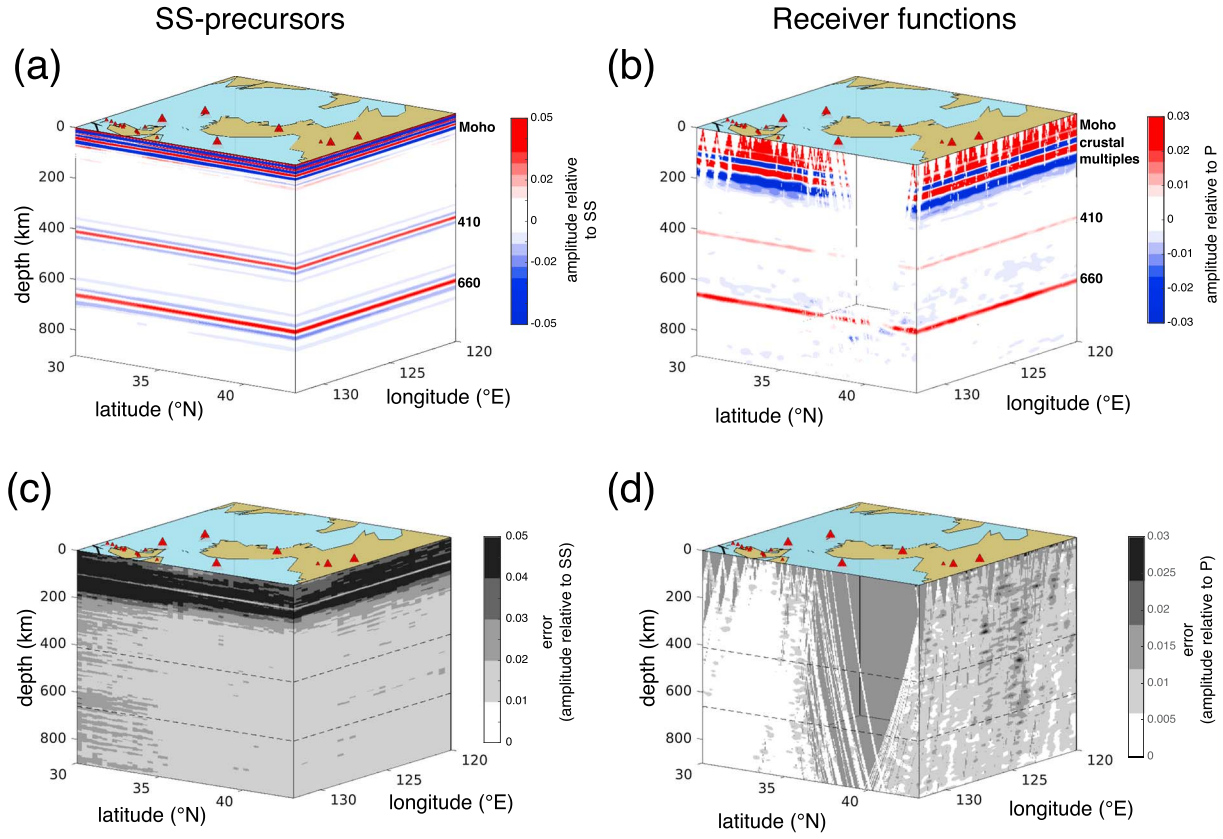

Figure 3. Seismic *cubes* for stacked signals along the 43°N and 132°E profiles. We show, respectively, the *iasp91* seismic structure obtained from the back projection of the synthetic (a) SS precursors and (b) receiver function data. We plot also the uncertainties on stacked amplitude computed from bootstrap resampling for the observations of (c) SS precursors and (d) receiver functions. Large red triangles in surface locate intraplate volcanic fields.

The latter is variable below the seismic arrays, low below the Korean permanent networks (< 0.5% the *P* wave amplitude) and, as expected, higher (between 0.5% and 1% the *P* wave amplitude) below the temporary array of portable stations NECESSArray in China. In all cases, the level of noise remains below the expected response from the MTZ structure in the iasp91 model.

To build maps of the topography of seismic boundaries, we follow the work of Tauzin et al. (2013) and Hier-Majumder and Tauzin (2017), where the topography is reconstructed from combining the information from CCP stacking along orthogonal profiles at intervals of 0.5° in longitude and latitude (see Hier-Majumder & Tauzin, 2017; Tauzin, Kim, & Kennett, 2017, for details). These profiles, shown in Figure S1c in the supporting information, achieve a fine coverage of the region. The number of data contributing to the stack along each profiles used for CCP stacking is heterogeneous (Figure 1d and Figure S1d in the supporting information) with a maximum southeast of the Korean peninsula. In section 4, we also discuss the effect of stacking RF data using a largely different parameterization, identical to the one used for stacking the SS precursors data set.

Depths to seismic interfaces are estimated from the depth distributions obtained from bootstrap resampling. For each profile, and each of the 100 bootstrapped CCP-stacked images, we pick automatically for the 410- and 660-km discontinuities the maximum of the stacked signals within the 350–500 km and 600–750 depth ranges. We obtain at each position *x* along the profiles a distribution of 100 depths of discontinuities (Figure 5a). These distributions may be normal, in which case their means and standard deviations are a meaningful measurement of the depth of interface and the measurement error. High standard deviations will often result from a high-level of uncorrelated seismic noise on the RFs or from uncertainties on the theory when, for instance, we use a 1-D velocity structure for back-projecting data that have sampled a heterogeneous 3-D structure. However, high standard deviations can also result from the complexity of the structure itself (e.g., Schmerr & Garnero, 2007). In the case of a broad velocity gradient, for example, we would expect a normal depth distribution with a large variance. If multiple seismic discontinuities are present with similar jumps in

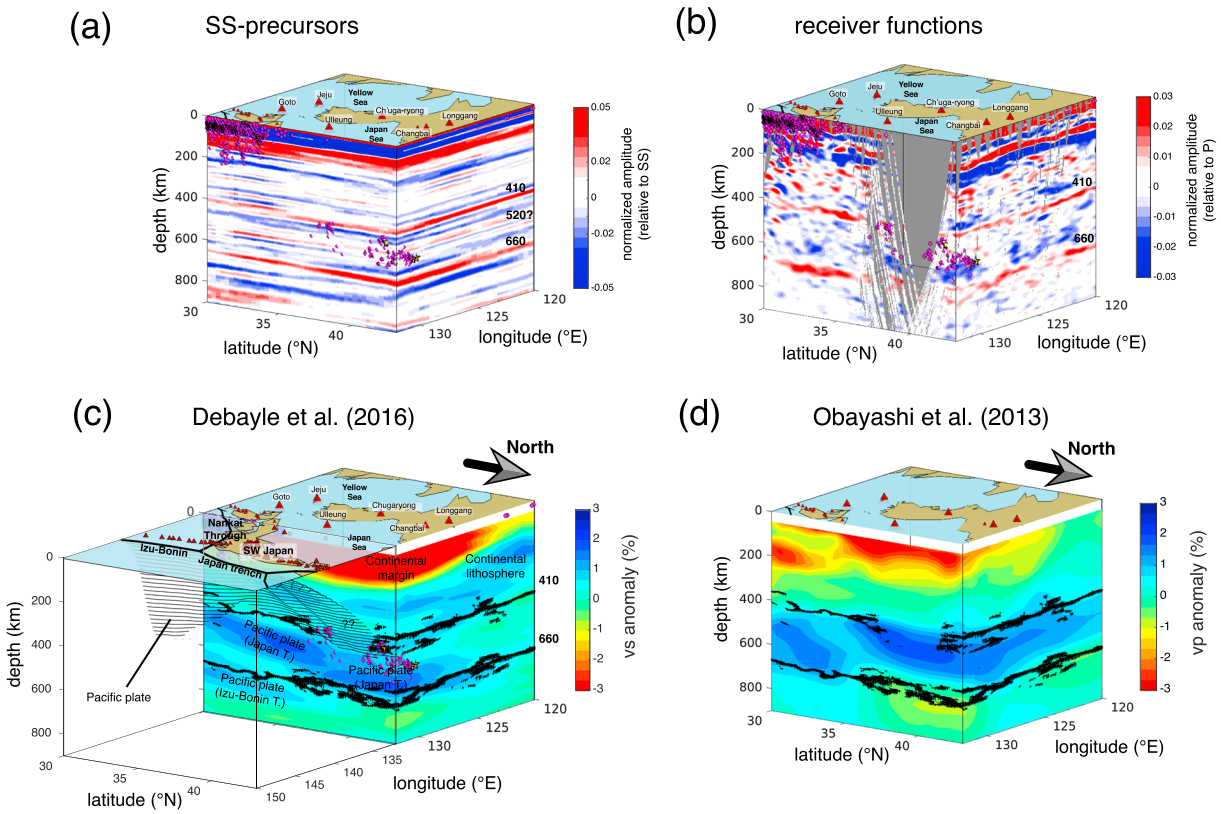

Figure 4. The upper mantle structure along the 43°N and 132°E profiles from converted and reflected body waves. We show, respectively, the seismic structure obtained from the back projection of (a) SS precursors data and (b) receiver function data and obtained from (c) surface wave seismic tomography (Debayle et al., 2016) and (d) *P* wave traveltime tomography (Obayashi et al., 2013). Structures corresponding to major velocity anomalies in the shear wave tomographic model are labeled in (c). We plot also in (c) the Pacific plate contours obtained from seismicity (Hayes et al., 2012). In both tomographic cross sections, black dots near 410- and 660-km depths represent the depth distributions of picked seismic interfaces obtained from receiver functions and bootstrap resampling. Magenta dots represent the seismicity. Large red triangles in surface locate intraplate volcanic fields.

shear wave velocity, picking with bootstrap resampling the maximum of discontinuity depth distributions will sample alternatively one of the few discontinuities, resulting in a multimodal depth distribution. In this case, the mean of the depth distribution is no more a meaningful measurement of the depth of interface. We estimate the depth of interfaces, shown in Figures S2a and S2c in the supporting information, by taking the depth at the maximum of the distribution. Taking one standard deviation of the depth distributions (Figures S2b and S2d) may not be representative of the true model uncertainties but potentially gives an indication on the complexity of the structure.

We provide our measurements of depths of the 410- and 660-km discontinuities and associated uncertainties in the supporting information (Figure S2). As we did not apply corrections for volumetric velocity heterogeneities, such measurements are biased by lateral variations of velocities in the lithosphere and cannot reliably be interpreted. We therefore focus on the MTZ thickness measurements (Figure 7b).

2.2. SS precursors (SdS)

Underside reflections of shear waves arriving as precursors to the SS phase are best observed on transverse components of three-component seismic stations (Shearer, 1991) and also provide a mean to study mantle velocity gradients under the SS bounce point (Figure 1b). We use 1-Hz sampled ground velocity measurement at global stations of the Global Seismic Network available from the Incorporated Research Institutions for Seismology for the period 1991–2009 (network codes: China Digital Seismograph Network [CD], Canadian National Seismograph Network [CN], GEOSCOPE [G], GEOFON Data Centre [GE], Global Telemetered Seismograph Network [GT], IRIS/IDA Seismic Network [II], Global Seismograph Network (GSN-IRIS/USGS) [IU], Mediterranean Very Broadband Seismographic Network (MedNet) [MN], United States National Seismic Network [US]) (for network information, see Albuquerque Seismological Laboratory (ASL)/USGS, 1986, 1988, 1990, 1993; GEOFON Data Centre, 1993; Geological Survey of Canada, 1989; GEOSCOPE, 1982; Med-

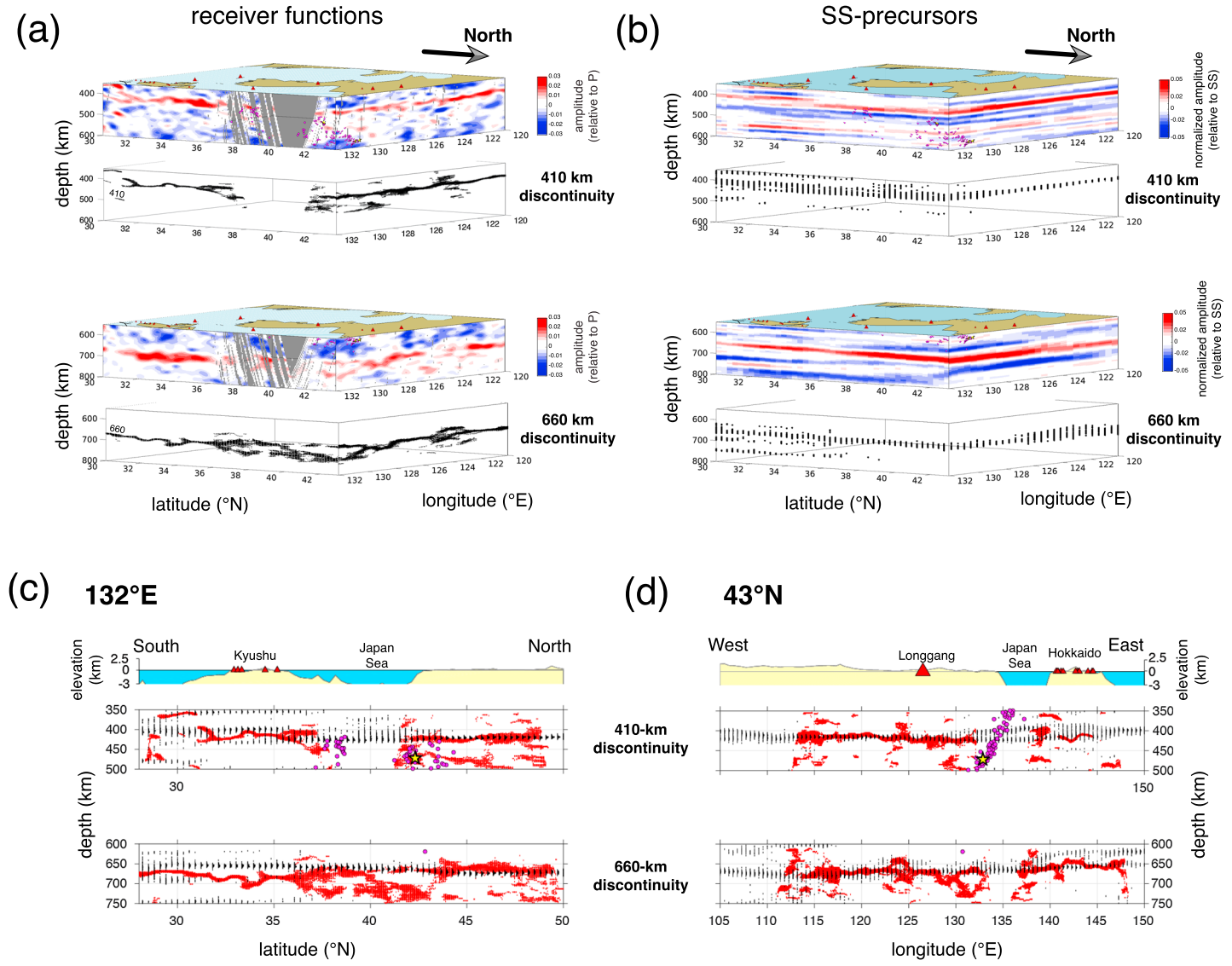

Figure 5. Apparent complexity of mantle transition zone boundaries. (a, b) Zoom over the mantle transition zone discontinuities for the profiles at 132°E and 43°N, with (upper panels) the raw seismic sections and (lower panels) the picking obtained from bootstrap resampling. (c, d) Direct comparison of observations of SS precursors (black histograms) and receiver functions (red histograms) for the apparent topography of the 410- (upper panel) and 660-km (lower panel) discontinuities. We superimpose the seismicity with all magnitudes (magenta circles) and magnitudes larger than 7.0 (yellow stars).

Net Project Partner Institutions, 1990; Scripps Institution of Oceanography, 1986). The data are obtained from earthquakes with magnitudes larger than 6.0. To avoid interferences with depth phases sSS and sSdS, with the topside multiple SS660S above the 660 (Figure 2a), the ScSScS reverberation (Figure 2a), and at large distances with waves traveling along the major arc, the depths of events are chosen shallower than 75 km and the epicentral distance between 110° and 170° (Flanagan & Shearer, 1998; Schmerr & Garnero, 2006). The seismograms are deconvolved from the instrument response and band-pass filtered with a zero-phase third-order butterworth filter between 10- and 75-s period. The shortest period is smaller than in typical global SS precursors studies (Deuss, 2009; Dokht et al., 2016; Flanagan & Shearer, 1998; Gu et al., 1998; Houser, Masters, Flanagan, & Shearer, 2008) but similar to regional studies from Schmerr and Garnero (2007) and Schmerr (2012), to increase the resolution. We provide in Figure S3 an illustration of the processing (shift in time, flip in polarity, and band-pass filtering) of a single earthquake record at station GRFO from the Incorporated Research Institutions for Seismology-U.S. Geological Survey global network (code IU, 1988).

The amplitude of precursors is weak, and the response of the structure rarely emerges from the noise level on individual seismograms (Figure S3). To improve the signal-to-noise ratio, our processing is in line with pro-

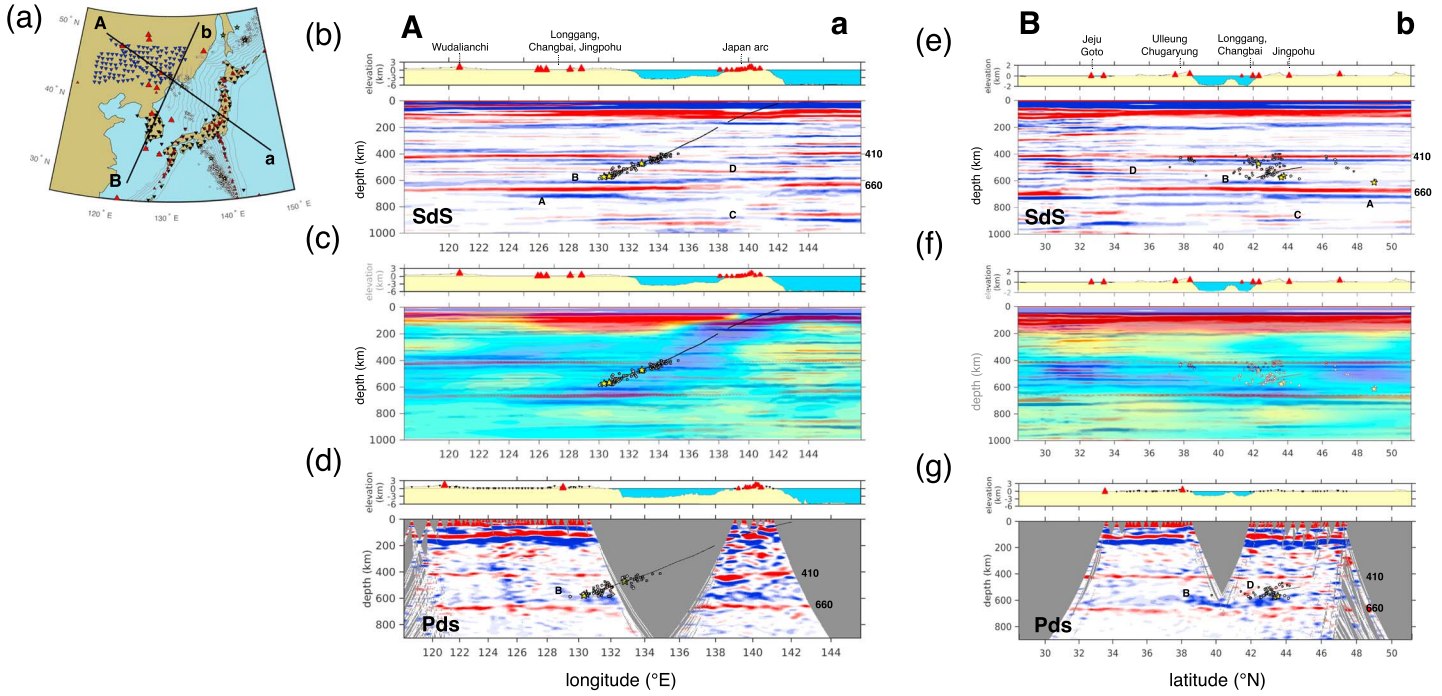

Figure 6. Large-scale imaging from SdS data and comparison with Pds data and surface wave tomography. (a) Location of two long-range seismic profiles (A-a and B-b) parallel and perpendicular to the Japan trench. Blue and black inverted, large red, and small red triangles locate seismic stations, intraplate, and arc volcanic centers, respectively. Circles locate the seismicity within the mantle transition zone. (b, e) Seismic sections obtained from SdS common reflection point stacking along the A-a and B-b profiles. We plot the plate contour from Hayes et al. (2012; black line) and the seismicity (dots and stars). Intraplate volcanic fields are labelled on the topographic profile at the top. The signals labelled A to D are discussed in the text. (c, f) Superimposition of cross sections through Debayle et al. (2016) surface wave tomographic model on top of the SdS seismic section. This reveals a clear correlation between large-amplitude negative signals on top and below the 660 (A and B) and the base of the Pacific plate. (d, g) Seismic sections obtained from Pds common conversion point stacking along the same A-a and B-b profiles.

cedures applied by Flanagan and Shearer (1998), Gu et al. (1998), Chambers et al. (2005), or Houser, Masters, Flanagan, et al. (2008). The seismograms are gathered by SS bounce points falling within bins with specific radius at the surface of the Earth. Then they are aligned on the SS phase and stacked with moveout corrections. The noise level is estimated from the ratio of the SS amplitude and a root mean square of the signal preceding the SS arrival. We discard data showing a ratio smaller than 5.

The efficiency of the stacking procedure depends on the reliability of the prior alignment of the seismograms on the SS waveforms. Prior studies have used manual alignment along the maximum of the SS waveform (Shearer, 1991), deconvolution of the entire record by the SS waveform (Flanagan & Shearer, 1998), or cross correlation of all seismograms with a same reference wavelet (Gu et al., 1998). Houser, Masters, Flanagan, and Shearer (2008) used a cluster analysis algorithm to assemble a catalog of high-quality SS waveforms. We adapt this method in a three-step procedure to achieve a good alignment of the SS waveforms associated with different earthquakes. This method increases data quality at the expense of data quantity, but this step is crucial as cycle skipping becomes a major issue when working at shorter period (10 s; e.g., Houser, Masters, Flanagan, & Shearer, 2008).

For each event, we measure the similarity of SS waveforms on the seismograms by windowing the SS phase and computing on this window a cross-correlation coefficient matrix (Sigloch & Nolet, 2006). The lags and signs of the maxima of the cross-correlated traces are applied to all traces to give them the same polarity and a first-order alignment on the SS waveform. We then apply a cluster analysis (Houser, Masters, Flanagan, & Shearer, 2008; Sigloch & Nolet, 2006) on a newly computed cross-correlation matrix to select the best quality data and refine the flipping and alignment of all traces. At this step, the SS alignment between waveforms corresponding to a same event is improved. Discrepancies still exist between SS waveforms from different events when gathering the data by common SS reflection points in bins at the surface of the Earth. To find a common reference time for the records associated with different events, we stack, for each event, the envelopes of the seismograms. The maximum of the average

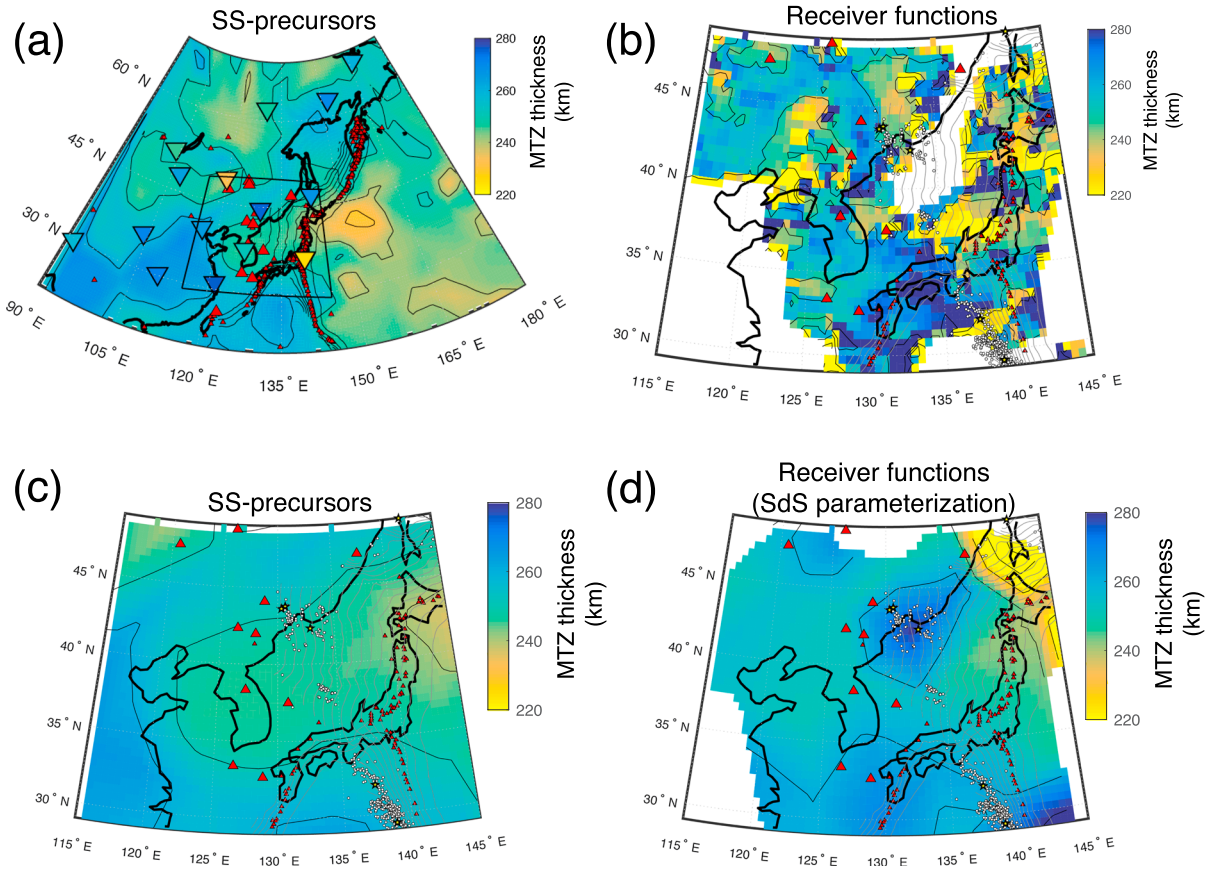

Figure 7. Comparison between SS precursors and receiver function observations. (a) Map of the variation of the MTZ thickness obtained from SS precursors (background) with, superimposed (inverted triangles), global observations of receiver functions from Tauzin et al. (2008). The black frame locates the region shown in (b–d) over which higher-resolution observation is achieved from regional receiver functions. The map is obtained from nearest-neighbor interpolation. (b) High-resolution map of the MTZ thickness obtained from the analysis of receiver functions at dense seismic arrays. Red triangles locate major arc and intraplate volcanic fields; the gray contour is the position of the Pacific plate in the mantle down to the MTZ, and deep seismicity in the MTZ is located with white dots. (d) Map of the MTZ thickness obtained from stacking the regional receiver function data set over the parameterization used for stacking SS precursors data. MTZ = mantle transition zone.

envelope gives a reference time associated with the SS arrivals for an individual event. The records associated with different events are then aligned using these reference times. The last step consists in applying the same cross correlation and cluster analysis on the data gathered by SS bounce points to align and flip in polarity the SS waveforms. The final data set comprises 5,027 SS bounce points in the large area shown in Figure 1c over a region extending between 20°N and 70°N in latitude and 90°E and 180°E in longitude. However, in the small region densely sampled by RF data (Figure 1d), the number of available SS precursors data decreases to 778.

Partially stacked observed and synthetic waveforms are shown in Figures 2a and 2c, for the small region sampled in Figure 1d. As for the RF data, we computed the synthetic transverse components for the iasp91 structure using the reflectivity algorithm from Fuchs and Muller (1971), the same acquisition geometry as in the observed data, and source mechanisms from the Global CMT catalog. In Figure S4, we show the processing of a synthetic waveform computed from the iasp91 structure. In addition to time shift, flip in polarity, and band-pass filtering, the processing applies a Hilbert transform (Figure S4) to the waveforms computed in the flat Earth's model to account for the $\pi/2$ phase shift due to phases encountering internal caustics in the mantle (Choy & Richards, 1975).

The acquisition geometry is not optimal for stacking, with a distribution of epicentral distances that suffers from a large gap beyond 155° (Figure 2). Despite the small number of stacked data in 1° epicentral distance bins, major seismic phases are clearly visible, in particular the S410S and S660S underside reflections around 160 and 230 s before the SS phase (Figures 2a and 2c). These phases remain visible when gathering and stacking the data in small 4° bins at the surface of the Earth (Figure S5). As in the Pds data, a weak positive arrival

is seen in between the S410S and S660S phases in the stack of observed data (Figure 2a), possibly associated with a reflection below the 520-km discontinuity (Shearer, 1996).

The negative sidelobes surrounding the SS, S410S, and S660S phases on the observed and synthetic data (Figures 2a and 2c) are common features in SS precursors studies. They result from variable *source functions*, a combination of the seismic source time functions, radiation patterns, and structure away from the bounce points. At long periods, even methods based on deconvolution are not able to completely remove these sidelobes (e.g., Flanagan & Shearer, 1998; Wei & Shearer, 2017). As discussed in section 3, these sidelobes do not prevent interpreting the general structure of the transition zone, although we note that they could slightly be reduced by using a less steep *roll-off* in the filtering process. The synthetics in Figure 2c and stacks of observed data within small caps at the surface of the Earth in Figure S5 do not indicate major distorsions near 120° epicentral distance, where the Sv660sSdiff phase is at least 50 s apart from the S660S phase. We do not expect strong interference with Sv660sSdiff as the epicentral distance distributions are generally skewed toward large epicentral distances (Figures 2a and S5). By stacking along the moveout curves for SdS, we also expect that phases with a different moveout (e.g., Sv660sSdiff, ScS660ScS, and ScS410ScS) interfere destructively.

The sensitivity of these data to depth perturbations of reflection interfaces is complex. Due to the mini-max traveltime character of the SS phase and precursors (Choy & Richards, 1975), the first Fresnel zone presents a distinctive shape in X, with arms reaching distances beyond 500 km from the specular reflection point (Shearer, 1991). By gathering and stacking seismograms with neighboring SS reflection points, with variable incidence angles and back azimuths, we expect to obtain a sensitivity which is approximately circular and nonnull on an extent similar to the size of the cells used for stacking (Gu et al., 1998; Lawrence & Shearer, 2008). When constructing seismic sections such as those shown in Figures 3a and 4a along the profiles at 132°E and 43°N, the parameterization consists of 100 circular cells with 4° radius, homogeneously distributed with a 0.3° step along the profiles. After time-to-depth conversion using the iasp91 model, we stack the corresponding SdS waveforms in the cells with bootstrap resampling. Again, our emphasis is to compare the results from different methods (Pds and SdS), image the local structure of discontinuities, rather than to obtain accurate absolute discontinuity depth estimates.

Figures 3a and 3c show the structure recovered from the iasp91 synthetic data and the error on the amplitudes (two standard deviations) obtained from the observed data. Compared with Pds phases, the advantage of imaging with precursors of the SS phase is that the image of the shallow upper mantle structure is not contaminated by multiple reverberations in the 100- to 200-km depth range (Figure 3a), those being recorded in a time window after the SS arrival. The 410- and 660-km interfaces are visible as a scaled version of the SS source wavelet (see Figure 2c, right panel), with amplitudes between 2.9–3.2% and 3.0–3.6% the SS phase. As the SS phases are aligned over the positive lobe of the source wavelet, the depth of interfaces must be measured on the positive lobe of the S410S and S660S phases (Figure 3a). The noise level on observed data (Figure 3c) decreases as expected as the square root of the number of stacked data. It does not exceed 3% of the SS amplitude and is larger south of 35°N.

For mapping the topography of discontinuities, we use an adaptive stacking approach (Lawrence & Shearer, 2008). We tesselate the Earth's surface with 188 nodes homogeneously distributed in the region of interest (Sambridge & Faletič, 2003; Wang & Dahlen, 1995; see Figures S1a and S1ab in the supporting information). These nodes are separated from their closest neighbors by a distance of $\sim 4°$. The radius of the cell associated with each node is initially defined so that it includes the 50 closest SS bounce points. After time-to-depth conversion, we stack the corresponding SdS waveforms with bootstrap resampling, picking on the 100 bootstrap samples the depth of interfaces within the 350–500 and 600–750 depth ranges. We expect that the error on the depth measurements decreases as the square root of the number of stacked data. We add to the stack the records associated with the 10 closest SS bounce points until the standard deviation on the depth distributions decreases below a threshold of ~5 km (Lawrence & Shearer, 2008). This operation results in maps of boundary topography with uncertainty (at the 68% confidence level) smaller than 5 km. The time-to-depth conversion is applied using the iasp91 reference structure (Kennett & Engdahl, 1991); therefore, our mapping does not account for systematic errors associated with the effects of 3-D variations in the velocity structure.

Figure S1a in the supporting information shows the average distance between SS reflection points in the cells and the node of the cells. As expected, the largest distances are obtained for cells located in the less densely sampled regions over the Eurasian continent at west and the Pacific Ocean at southeast (see Figure 1c). These distances can locally reach 10°, a distance that is typically used as a radius for stacking SS precursors data at

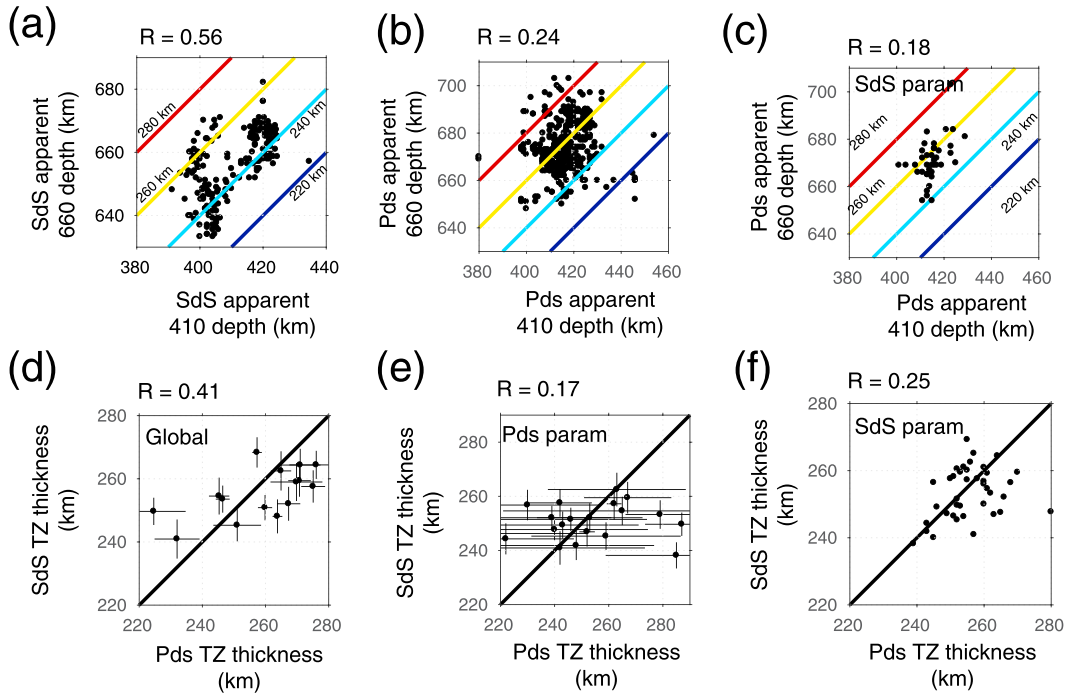

Figure 8. Correlation plot for SdS and Pds observations for the 410 and 660 apparent topographies (a–c) and the TZ thickness (d–f). (a) Correlation between the apparent depths of the 660 and 410 obtained from SS precursors. The Pearson correlation coefficient is indicated at the top. Data points falling along the diagonal colored lines are associated with the corresponding value of transition zone thickness. (b) Correlation between the apparent depths of the 660 and 410 obtained from regional observations of Pds receiver functions. We plot only the observations for which the standard errors are smaller than 10 km. (c) Correlation between the apparent depths of the 660 and 410 obtained from regional Pds observations but stacked over the same parameterization as used for stacking SS precursors data. (d) Correlation between TZ thickness observations from SS precursors and global measurements of Pds phases of Tauzin et al. (2008). (e) Correlation between TZ thickness observations from SS precursors and regional measurements of Pds phases. (f) Correlation between TZ thickness observations from SS precursors and the regional measurements of Pds phases over the same parameterization as for stacking SS precursors data. TZ = transition zone.

a global scale (e.g., Flanagan & Shearer, 1998; Gu et al., 1998). However, in most parts of the region, distances are below 5° and can locally reach ~ 3° in northeast China and the northwest of the Pacific Ocean. Our choice of using fixed 4° radii cells for stacking the data along the 132°E and 43°N profiles and making the seismic *cube* shown in Figure 4a is therefore in agreement with the resolving power (noise) of the data. To satisfy the imposed maximum level of uncertainty of 5 km, the number of data gathered and stacked in the cells is highly variable (Figure S1b in the supporting information).

The absolute topography measurements are biased by lateral variations of velocities in the lithosphere. We therefore discuss only our MTZ thickness measurements (Figures 8a and 8c). The maps of absolute topography are shown with standard errors in Figure S6 in the supporting information.

3. Results

3.1. General Mantle Structure

The general structure of the mantle is shown in the seismic cubes of Figure 4, with a zoom over the MTZ boundaries in Figure 5 and larger-scale images along two profiles in Figure 6. We compare SdS and Pds observations with the shear wave velocity structure (*vs*) obtained from a global surface wave velocity model (Debayle et al., 2016), the compressional velocity structure from a global body wave traveltime tomographic model (Obayashi et al., 2013), and the distribution of deep-focus earthquakes from the U.S. Geological Survey catalog.

The structure in the MTZ in the tomographic models (Figures 4c, 4d, and S7) is dominated by the presence of fast velocity anomalies with +2% to +3% amplitudes, except in the global *vs* model below the continental portion of the profile at 43°N and between 120°E and 125°E, where the *vs* structure is close to its average or slightly slower (−1%). Along this same 43°N profile (Figure 5d), in a direction almost orthogonal to the Japan

trench (Figure 1d), the seismicity distribution is typical of a Wadati-Benioff zone. It marks the Pacific plate in subduction below Hokkaido, reaching and extending into the MTZ northwest of the Japan Sea, as evidenced by the seismic tomography in Figures 4c and 4d. Although broader, the zone of normal to slower *vs* velocities seen at ~ 125°E (Figure 4c) coincides in location with an interpreted region of hot and buoyant upper mantle plume (Tang et al., 2014). However, this zone of slower than average velocities does not manifest in the global teleseismic *P* wave model (Figure 4d).

The structure sampled along the 132°E profile is more complex (Figure 1). To the south, the shallow subduction of the Philippine Sea plate in the upper mantle below Honshu is attested by the shallow to intermediate depth seismicity (Figure 4c). To the south also, a fast velocity anomaly is stalled at the base of the MTZ below Honshu and the Philippine Sea plate, between 600- and 800-km depth in Figures 4c and 4d. It likely corresponds to the portion of the Pacific plate subducted at the Izu-Bonin trench. At north the Pacific plate, in subduction from the Japan trench, reaches the MTZ beneath the Japan Sea and dips gently toward the north (Figure 4c). Due to a projection effect along this profile, the Wadati-Benioff zone in the MTZ has a complex shape in *wedge* (Figures 5c and S7).

In the MTZ (Figures 4a and 4b), our seismic images reveal continuous interfaces in red that are the expression of solid-solid mineralogical phase changes with the major 410- and 660-km boundaries and possibly a 520-km interface, visible by intermittence in the SS precursor data (labeled). The absolute depths of seismic interfaces obtained from RF and SS data agree relatively well. Figures 5c and 5d compare these distributions within the 350- to 500-km and 600- to 750-km depth ranges. The structure appears more complex from RF data (red distributions) than from SdS data (black distributions). However, both distributions are centered near a similar depth. This observation is striking given the different intrinsic lateral resolution, sensitivity of each method (~800 km for SdS and ~150 km for Pds), and the absence of correction for shallow volumetric velocity variations. There is an exception, between 32°N and 37°N, where the 660 discontinuity from SdS appears ~50 km shallower than observed with Pds data (Figure 5c). At this location, however, bootstrap resampling on SdS data captures a minor interface near 690-km depth, which appears compatible with the interface observed from Pds data (Figure 5c).

The MTZ (Figure 5) and more generally the upper mantle as a whole (Figures 4 and 6) show significant complexity that the iasp91 radial structure is not able to reproduce (Figures 3 and S8). This complexity affects the major 410- and 660-km boundaries, as evidenced by the picking obtained from bootstrap resampling on both Pds and SdS observations (Figures 5a and 5b), and also the background structure within the MTZ as we observe large zones of negative amplitude (Figures 4 and 6), inexistant in the synthetic data (Figures 3 and S8).

3.2. Multiple Seismic Discontinuities

The most striking feature is the apparent doubling of the 660-km discontinuity shown by the RFs between 36°N and 44°N in Figures 5a and 5c. This feature has previously been reported in the RF studies from Niu and Kawakatsu (1996), Ai and Zheng (2003), and Tian et al. (2016). The cross section along the orthogonal direction, at 43°N (Figures 5b and 5d), shows that this doubling is narrowly distributed over 3° in longitude, meaning that if an isolated *pocket* of mantle rocks with contrasting elastic properties exists, it has a size of 890×350 km^2.

A feature that has not been reported in previous work (Liu et al., 2015; Niu & Kawakatsu, 1996; Tian et al., 2016) is the similar level of complexity on the 410-km discontinuity. In the RF data (Figures 5a and 5c), the 410-km boundary seems to split into two portions near 35°N, one at a similar depth of ~410 km and the other dipping gently toward the north. The *splitting* near 35°N latitude (Figures 5a and 5c) occurs in the area of coverage of the F-Net network in Japan, whereas the doubled 410 beneath northeast China is imaged with the NECESSArray portable seismic experiment. Both deep segments, south and north of the Japan Sea, are in prolongation of the one to the other so we expect that this apparent structure extends across the Japan Sea. The large gap in ray coverage near 135°E and 40°N makes, however, the discussion of its lateral continuity difficult and likely explains the absence of such a report in previous studies. Some complexity exists also locally on the 410 and 660 near 125°E along the 43°N profile (Figures 4b–4d and 5a). Possibly fortuitously, it coincides geographically with the zone of slow velocities in the MTZ interpreted as a hot mantle upwelling (Tang et al., 2014).

In general, if MTZ boundaries show some level of complexity in the SdS data, this complexity shares little similarity with the one observed from Pds data (Figure 5). This is possibly a consequence of a difference in cov-

erage and sensitivity of both data types. In particular, the 890×350 km^2 region of doubled 660 discontinuity observed with the RFs (Figures 5b and 5c) should hardly be visible with SS precursors because its size is near the minimum required for SdS resolution (e.g., Schmerr et al., 2013; Shearer et al., 1999). In addition, any positive velocity gradient will show negative lobes on both sides of the positive amplitude reflection, further reducing the resolving power of SdS data in case of multiple seismic interfaces.

3.3. Negative Amplitude Zones

In addition to the complexity on the MTZ boundaries themselves, we find large zones of negative amplitude in Pds and SdS images (Figures 4a and 4b, 5a and 5b, and 6), suggestive of downward negative velocity gradients within and surrounding the MTZ. These zones have been previously reported in RF studies from Shen et al. (2008), Gao et al. (2010), and Liu et al. (2015) and made the object of an analysis in a recent RF study from Tauzin, Kim, and Kennett (2017).

As discussed by Tauzin, Kim, and Kennett (2017), these negative amplitude zones in RF data do not result from uncorrelated noise on RFs or multiple reverberations in the shallow upper mantle structure. Their independent detection here using SS precursors data that are less subject to contamination from multiple reverberations reinforces this conclusion. Some ambiguity, however, still persists as the deconvolution process for building the RFs may introduce sidelobes, and the source wavelet, which is convolved to the reflectivity structure in SdS observations, has almost symmetric negative sidelobes around the main central lobe (see the SS phase in Figures 2a and 2c). The synthetic images from RF in the iasp91 structure in Figure 3b show negative signals within the MTZ but, as discussed by Tauzin, Kim, and Kennett (2017), their amplitudes are weak, one third of observed on the data.

Given the parameterization and level of smoothing of SdS images, these negative zones appear narrowly focused in depth and elongated in the horizontal direction, whereas Pds data show more pervasive features with larger depth distributions. In SdS synthetic sections (Figure 3a), apart from the weak negative sidelobes surrounding the 410 and 660, there is no indication of significant large-amplitude artifacts. Moreover, the negative amplitude zones do not seem to result from contamination/pulse distorsion related to the interference of the Sv660sSdiff phase near 115–125° epicentral distances, as in general these distances contribute little to the stacks (Figures 2a and S5). In addition, for bins where the epicentral distance is skewed toward 115–125°, we do not systematically find a negative feature beneath or above the S660S (Figure S5a).

The most compelling evidence for structural complexity in the MTZ is provided by the large-scale images along the A-a and B-b profiles shown in Figure 6. These images further confirm that the general character of the MTZ reflectivity varies as a function of depth as well as laterally. Tauzin, Kim, and Kennett (2017) suggested that the negative zones of reflectivity in RF data are associated with subducted plates in the MTZ. This interpretation is supported by the observation that in the SdS sections, the strongest negative amplitude zones at the base of the MTZ (labeled A and B in Figures 6b and 6e) coincide with the base of the tomographic fast-velocity anomalies from the Pacific plate (Figures 6c and 6f). In addition to these negative amplitude zones and the 410, 660, and 520 discontinuities (labeled D in Figures 6b and 6e), the SdS data also reveal interfaces near 900-km depth (C in Figures 6b and 6e) compatible with prior observations of source side *S*-to-*P* scattering in the uppermost lower mantle (Niu, 2014).

3.4. Apparent Discontinuity Topography

In general, correcting apparent topography (or the MTZ thickness) for lateral volumetric velocity variations in the mantle requires caution because an artificial correlation can be introduced in the otherwise uncorrelated data (Chevrot et al., 1999). This is especially the case when the corrections are based on global-scale linearized tomographic reconstructions with some level of damping and smoothing, low resolution and generally underestimating the amplitude of velocity anomalies. It is likely that the resolution of global surface wave tomography is sufficient for correcting SdS observations but not sufficient for correcting regional Pds observations (e.g., Tauzin, Kim, & Kennett, 2017). Regional body wave traveltime tomography might provide sufficient lateral resolution for correcting Pds observations, but this type of model does not presently cover the entire study region. Therefore, to provide an unbiased view of our Pds and SdS measurements, we do not correct for lateral velocity variations. In this context, the MTZ thickness is expected to be a more representative proxy for the effect of temperature on olivine phase changes than absolute topography (Tauzin & Ricard, 2014).

Maps of apparent topography of the 410- and 660-km discontinuities are shown with associated uncertainties in Figures S2 and S6 in the supporting information. In general, our observations for RFs are in good agreement with prior observations from Niu et al. (2005), Lee et al. (2014), and Liu et al. (2015). The only high-resolution regional SS precursors studies describing the MTZ structure beneath the northeast Asia margin are from Gu et al. (2012) and Dokht et al. (2016). They do not provide maps of absolute topography. We find that regions with the sharpest lateral variations in topography are also associated with the largest uncertainties. This occurs mainly in the limit of data coverage (Figures S2 and S6). Large RF uncertainties (Figure S2) are also the result of a complex structure, such as the doubling of the 660-km discontinuity between 36–44°N and 130–133°E.

The apparent 410 and 660 topographies from both datasets are positively correlated (Figures 8a and 8b). This is a direct effect of lateral variations of velocities above the MTZ that are not corrected for and thus mask the negative correlation expected from the effect of temperature on the stability of the olivine polymorphs (e.g., Tauzin & Ricard, 2014). The Pearson correlation coefficient is +0.56 for SdS. The correlation for regional Pds data is surprisingly small (+0.24; Figure 8b). This behavior is opposite to what is found at a global scale (see Chevrot et al., 1999), where the correlation is 3 times larger for Pds (+0.93) than for SdS. In addition, the correlation from Pds phases in the northeast Asia margin is 2.5 smaller than observed in the western United States (+0.6; Tauzin & Ricard, 2014). These observations suggest that the effect of shallow velocity heterogeneities in the crust and lithosphere is predominant when sampling the Earth at global/large scale but more variable at regional scale: locally, below the northeast Asia margin, the variation in MTZ structure (background velocities and 660 topography) is strong enough to suppress the positive correlation between the 410 and 660 topographies, whereas in the western United States, the heterogeneity in MTZ structure is not strong enough to compensate the effect of shallow velocity structure.

3.5. MTZ Thickness

Figures 7a and 7c show raw maps of MTZ thickness obtained from the SdS data. The average thickness is 245 km, with 10-km standard deviation and 41-km peak to peak variations. These variations are of the same order of magnitude as those observed in global SdS studies (Flanagan & Shearer, 1998; Gu et al., 1998). The thickest MTZ (269 km) is found near 112°E below south-central China where tomographic models suggest the presence of the Pacific plate stalled within the MTZ (Debayle et al., 2016; Huang & Zhao, 2006; Li & Van Der Hilst, 2010). The minimum thickness, 228 km, is found in the Pacific, east of Hokkaido. There is good agreement between large-scale patterns of thick/thin MTZ and average patterns of fast/slow shear wave velocity anomalies in the transition zone in the global shear wave velocity model of Debayle et al. (2016; Figure S9). Dokht et al. (2016) performed an SdS waveform inversion to simultaneously constrain the shear wave velocities and the thickness of the MTZ in the region enlarged in Figure 7c. Our observations of thickness are in agreement beneath the Korean peninsula and northeast China, but there is a large difference at the limit of their study area, northwest of the Yellow Sea, where they find a thin MTZ (~230 km).

Figure 7b shows the map of MTZ thickness obtained from the regional Pds data. Over the study region, the average thickness is 250 km with 30 km standard deviation, but if we consider only observations with uncertainties smaller than 10 km, the average and standard deviation change to 258 and 14 km, respectively. The patterns are in good agreement with previous observations by Niu et al. (2005), Lee et al. (2014), and Liu et al. (2015). In particular, we find a large region of thickened MTZ over southwest Japan (~285 km). The MTZ decreases in thickness (~260 km) toward the Korean peninsula at northeast. The MTZ in northeast China is moderately thick (~260 km) except beneath the Songliao Basin where it appears thinner (down to ~220 km). This thinning, together with slow-velocity anomalies within the MTZ (see Figures 4c and S7), was interpreted as the signature of a hot mantle plume (Tang et al., 2014). The 410 and 660, however, exhibit significant complexity in this region (Figure S2).

In Figures 7a and 8d, we compare our SdS with global Pds observations (Tauzin et al., 2008). There is a modest agreement with a positive Pearson correlation coefficient of +0.41. In Figures 7b and 7c, we compare the MTZ thickness measurements from SdS with the higher-resolution regional Pds observations. Qualitatively, there is some spatial agreement between both maps, with a thicker MTZ south of Japan, a band of thicker MTZ in the northwestern corner of the study region, and a thinner MTZ toward the north of Japan and the Pacific Ocean. However, although positive, the correlation is almost insignificant (0.17). As expected due to the spatial sensitivity of the data, most of the variations in MTZ thickness are observed on Pds data (Figure 8e). In Figure 7d, we show the result of stacking the regional RF data over the parameterization used for stacking the SdS data, that is, the 188 homogeneously distributed circular cells with variable radii. This crude processing of

the RF data allows restituting larger-scale variations in the MTZ structure and improves the spatial correlation with SdS data (+0.25; Figure 8f). The correlation coefficient is reduced by the region of thickened MTZ centered at 43°N and 133°E in Pds data (Figure 7d), absent from the SdS data (Figure 7c). Fortuitously, this region of thickened TZ is centered below the deepest cluster of seismicity beneath the northwest of the Japan Sea (Figure 7d).

4. Discussion

The use of two approaches of teleseismic imaging, namely, *P*-to-*S* RFs and SS precursors provides independent constraints on the nature of seismic gradients within the MTZ. In absence of seismic anisotropy and for the incidence angles considered here, the compressional-to-shear wave-converted field has a polarization in the vertical plane of the sources and receivers and is mainly sensitive to the v_s structure. The SdS-reflected wavefield analyzed on the transverse components has a polarization in the horizontal plane and is mostly sensitive to variations in the shear impedance contrast ρv_s, where ρ is the density. The effects of anisotropy, dipping interfaces, and diffractions are expected to complicate the measured wavefield in terms of polarization and traveltime. These effects can be expected in the 3-D heterogeneous subduction system in the northeast Asia margin, where multiple slabs dip with varying angles and plate fragments have been documented. These effects, however, are difficult to assess without extensive numerical modeling in three dimension (e.g., Monteiller et al., 2012). Three-dimensional prestack Kirchhoff depth migration (e.g., Cheng et al., 2017; Millet et al., 2017) may also offer the opportunity of improving our images with suitable base velocity models.

4.1. Complexity of the MTZ

We document spatial variations in the depth of reflection/conversion at discontinuities in the northeast Asia margin. Although we did not apply corrections for the shallow velocity structure, we find consistency in the average depths of the 410- and 660-km discontinuities from both SdS and Pds data. However, compared to Pds, the pattern in topography from SS precursors is larger scale unless we stack the Pds data over a similar parameterization (Figure 8). This is not new and has been demonstrated at a global scale by Lawrence and Shearer (2006). This difference results from the different sensitivity of the seismic probes to mantle boundary topography and volumetric velocity heterogeneities and also certainly to the parameterization and regularization used in the imaging principle. Reconciling these two data sets is achievable provided that we better account, theoretically and numerically, for their sensitivity to the 3-D structure (e.g., Koroni et al., 2017; Lawrence & Shearer, 2008), consider regions with good data coverage, and design parameterizations that account for the heterogenous data sensitivity and coverage (Tauzin, Afonso, et al., 2017).

We also document spatial variations in the reflective properties of the discontinuities. Instead of being simple first-order boundaries, they rather seem to correspond to broad zones of velocity gradients, with doubled or multiple first-order discontinuities (see Figures 4 and 5) over some areas. We focus here on the 660-km discontinuity observed from RFs. As reported in previous studies (Ai & Zheng, 2003; Liu et al., 2015; Niu & Kawakatsu, 1996; Tian et al., 2016), we find a complex 660 over a 890 × 350 km^2 rectangular region between 36–44°N and 130–133°E at the tip of the subducted Pacific plate in the MTZ. This complexity must be considered with caution as it is located in a region of reduced coverage in Pds piercing points (Figure 1c), with larger uncertainties (Figures S2b and S2d). Our bootstrap analysis suggests, however, that the average amplitude of these signals exceeds the confidence level at 65%. By changing the size of the binning and the parameterization for CCP stacking, Tauzin, Kim, and Kennett (2017) tested if they could identify a bias due to the projection of 3-D structure on to the 2-D plane of the profile. But they found that the general signature of the 660 did not change much throughout this zone. In addition, we show in Figure S10 in supporting information that individual waveforms of Pds waves converted at the 660-km discontinuity in this rectangular region are complex, sometimes multimodal, suggesting that the multiple interfaces observed in the CCP stacking are not the result of stacking out-of-phase signals. The slowness of the phases does not deviate much from the one from conversions (Tauzin, Kim, & Kennett, 2017), also suggesting limited effects of reverberations in the shallow structure or wave interference.

4.2. What Mineralogical Models Tell Us About the Observed Complexity

Ai and Zheng (2003) proposed that the phase changes in the garnet-pyroxene component of the mantle, from garnet-to-ilmenite and ilmenite-to-perovskite, are at the origin of the multiple signals at the base of the transition zone in this region. In Figure 9, we show a diagram of the shear wave velocity gradients expected for a pyrolitic-like model (Baker & Stolper, 1994). We computed phase equilibria assemblages and all their rele-

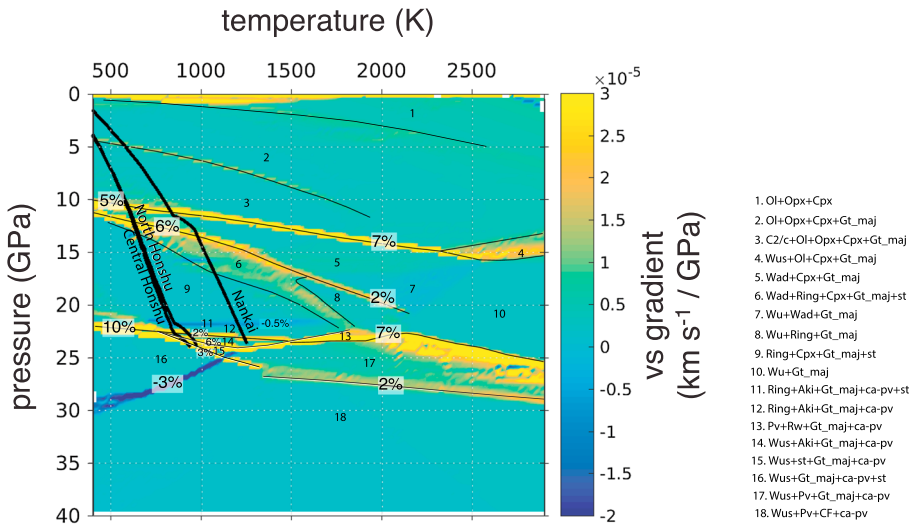

Figure 9. Shear wave velocity gradients (background color) plotted as a function of pressure and temperature for a pyrolite model of mantle composition (Baker & Stolper, 1994). Yellow and blue colors mark downward increase and decrease of v_s, respectively. Thin black lines locate major phase boundaries. The values in percentage represent the effective shear wave velocity contrast across these phase changes. The numbers are associated with the mineralogical phase assemblages listed at the right. We superimpose three geotherms (thick black lines) associated with plate subduction at the North Honshu, Central Honshu trenches, and at the Nankai trough, based on a thermokinematic subduction model (Negredo et al., 2004) and subduction parameters from Syracuse et al. (2010).

vant physical properties, as functions of pressure, temperature, and bulk composition via Gibbs free-energy minimization. We adopted the internally consistent database and thermodynamic model of Stixrude and Lithgow-Bertelloni (2011) and used components of the software Perple_X (Connolly, 2009) to perform the minimization and extraction of physical parameters within the system Na_2O-CaO-FeO-MgO-Al_2O_3-SiO_2. The phase diagram shown in Figure 9 is similar to those presented in Stixrude and Lithgow-Bertelloni (2011) and Faccenda and Dal Zilio (2017), obtained with a different software. We superimpose on this phase diagram approximate pressure-temperature (P-T) paths for the Nankai and North and Central Honshu subduction zones that have been obtained from the extrapolation of shallow subduction thermal models to the depths of the MTZ. The heat transfer equation is solved using a finite difference algorithm (Negredo et al., 2004), with the shallow geometry of plate subduction (dip angle), the plate subduction velocity, and the age of subducting plate prescribed as given by Syracuse et al. (2010). In North Honshu, we checked that the geometry of the resulting thermal model fitted the Wadati-Benioff zone down to approximately 550-km depth. The minimum temperatures expected in the plates at 660-km depth are roughly 1200 K for the Nankai slab, 800–900 K for North and Central Honshu slabs, sampling the coldest portion of the phase diagram (Figure 9). We acknowledge that these estimates are subject to relatively large uncertainties as they all depend on uncertain parameters, in particular the trench location at the time of subduction, the age of the plate, the subduction velocity, and its exact geometry (e.g., Liu et al., 2017; Yang et al., 2018).

The phase equilibria in Figure 9 are significantly more complicated than the ones for simpler Mg_2SiO_4 (olivine) or Mg_2SiO_3 (pyroxene-garnet) systems which are typically used for interpreting seismic observations in terms of mineralogy (e.g., Ai & Zheng, 2003; Cottaar & Deuss, 2016; Deuss et al., 2013; Simmons & Gurrola, 2000; Tauzin & Ricard, 2014). The first and most obvious observation in Figure 9 is the complexity of the phase diagram and velocity gradients for temperatures compatible with the subduction in Central and North Honshu (~1000 K). At pressures of the base of the MTZ (~23 GPa), multiple positive v_s gradients (reactions 12–14, 14–15, and 15–16 in Figure 9) involve the minerals ringwoodite (Ring), the garnet-majorite (Gt_maj), the Ca-perovskite (ca-pv), the akimotoite (Aki), the Mg-perovskite (Pv), the calcium-ferrite (CF), and the stishovite (st). These three reactions result in 2%, 6%, and 2% v_s contrasts respectively, and occur within an interval of pressure of 0 GPa near 700 K and 3.5 GPa (~75 km) near 1300 K. We can expect that the combination of such gradients would give either broad waveforms or distinct pulses of conversions and reflections at the base of the MTZ, as proposed by Simmons and Gurrola (2000), Ai and Zheng (2003), and Tauzin and Ricard (2014). In general, the response of the 660-km discontinuity with respect to temperature is relatively flat, suggesting a

small effective Clapeyron slope, except in the hot part of the diagram (> 2000 K) where the transition in the majorite-garnet is broad with a positive Clapeyron slope (Deuss et al., 2006; Hirose, 2002; Tauzin et al., 2008). A weak (~2%) secondary positive v_s gradient corresponding to the complete dissolution of majorite-garnet (Gt_maj) in the Calcium-perovskite (ca-pv) occurs near 28 GPa in this part of the diagram. The results in Figure 9 indicate that multiple seismic discontinuities with maximum separations of ~80 km, such as those observed in our data (Figures 4 and 5), can exist near the base of the MTZ if the local temperature is around 1000–1300 K.

In the cold portion of the phase diagram (Figure 9), complexity exists also in the uppermost part of the MTZ. The reactions 5–6 and 5–8 in the mid-MTZ are associated with the transitions from wadsleyite (Wad) to ringwoodite (Ring). The sharpness and amplitude of the v_s contrast across these phase changes increase with decreasing temperature. The depth of the transition decreases also with decreasing temperature to the point that the separation between the olivine-wadsleyite (the 410-km discontinuity; reaction 3–5) and wadsleyite-ringwoodite (the 520-km discontinuity; 5–6) transitions is close to 1.5 GPa (~30 km) at 750 K. Therefore, the cold temperatures indicated by the slab geotherms in Figure 9 could explain, at least partly, the observed complexity in the upper part of the MTZ in Figures 4b and 5 (see also Tian et al., 2016).

The present compositional (Baker & Stolper, 1994) and mineralogical (Stixrude & Lithgow-Bertelloni, 2011) models suggest the stability of stishovite (st), a high-pressure polymorph of SiO_2, at pressures pertaining to the base of the MTZ (Figure 9). Stishovite is indeed present in a small proportion at all depths and at temperatures below 1800 K in several mineralogical assemblages (phases 6, 9, 11, and 16 in Figure 9; see also Stixrude & Lithgow-Bertelloni, 2011). Of all MTZ minerals, stishovite has the largest known isotropic elastic velocities (Stixrude & Lithgow-Bertelloni, 2005). The disappearance of stishovite in reactions 11–12 and 16–18 is accompanied by a decrease in both shear and compressional wave velocities. In contrast, the density of the mineral assemblages increases across these transformations. To our knowledge, this is the first time that these reactions are analyzed and compared to seismic observables in the context of the thermochemical structure of the MTZ. If confirmed, the presence of stishovite could explain the presence of these low-velocity zones atop the 660-km discontinuity and in the uppermost lower mantle in cold environments.

Pervasive zones of low-seismic velocities have been found near 590- to 600-km depth below the northeast Asia margin in association with stagnant plates in the MTZ (Gao et al., 2010; Liu et al., 2016; Shen et al., 2008; Tauzin, Kim, & Kennett, 2017). Similar seismic signatures have been found in the tectonically active part of western Unites States in association with the subducted Farallon plate (Eager et al., 2010; Tauzin et al., 2013; Zhang et al., 2018). These zones are hardly explained by the thermal signature of subducted plates alone (Tauzin, Kim, & Kennett, 2017). The phase equilibria in Figure 9 suggest that the disappearance of stishovite in reaction 11–12 occurs at an almost constant pressure of ~22 GPa with a weak reduction of v_s (−0.5%) over the 750 to 1750 K interval of temperature. This pressure is consistent with the depth of 590–600 km inferred for the top of the low-velocity zones in western United States and northeast Asia. The predicted velocity jump across the phase change is weak and makes the interface hardly detectable with the present data. However, the reflectivity may be enhanced if stishovite is stable in larger proportion through accumulation of subducted oceanic crust at the base of the MTZ (Shen & Blum, 2003; Shen et al., 2014).

Sharp reductions of velocities have been reported near 750-km depth in the lower mantle below western United States and the northeast Asia margin (Liu et al., 2016; Schmandt et al., 2014). They have been attributed to partial melting of mantle rocks due to the dehydration of MTZ minerals when entrained into the lower mantle within downward convective limbs of mantle convection. In cold MTZ scenarios (e.g., affected by the subduction of cold slabs), we propose here an alternative scenario. At temperatures below 1200 K, compatible with subduction in northeast Asia, the disappearance of stishovite in reaction 16–18 is accompanied by a strong v_s reduction (−3%) and could therefore explain the presence of a low-velocity zone. The Clapeyron slope of this transformation is large and negative, −5 GPa for 600 K, that is, roughly −8 MPa/K, with the potential of explaining low-velocity zones at various depths in the uppermost lower mantle. An independent marker for the presence and disappearance of stishovite would be either the presence of a multiple or complex 660-km discontinuity (reactions 12–14, 14–15, and 15–16), such as imaged in Figure 4, or a unique but quite large positive jump in v_s (~10%; reaction 9–16).

The model of stishovite stability is an alternative model for explaining low-velocity zones in cold MTZ settings. In western United States, it is worth considering if the ~1200 K temperatures would be plausible given the plate age and time since subduction for slabs in that region. The sharp reductions of velocities near 750-km depth have been reported east of the Rocky Mountains, beyond 105°W longitude (Schmandt et al.,

2014). Plate reconstruction models (e.g., Müller et al., 2008) indicate that, in this region, the Farallon plate was ~30 Myr old at the time of subduction, 50 to 60 Myr ago. This is significantly younger than the ~130 Myr of the plate in subduction at the Japan trench (Liu et al., 2017; Syracuse et al., 2010). The P-T path for such a former subduction zone should therefore be significantly hotter than in northeast Asia, which would discard the scenario described above.

The presence of various phase transitions around 660-km depth, each dominant at different temperatures, may allow us to use the 660-km discontinuity as a thermometer for absolute temperature. Indeed, the phase diagram in Figure 9 suggests that subtle variations in temperature, for instance, from 1000 to 1300 K, affect the reflectivity of both the shallowest olivine-controlled phase and the deepest garnet-controlled phase boundaries near 660-km depth. Also, for basalt and harzburgite mixtures that have not reach chemical equilibrium, increasing the basalt fraction enhances the velocity contrast across the deep garnet phase boundary, at the expense of the contrast across the shallower olivine boundary (e.g., Zunino et al., 2016). The lateral variations of relative amplitudes of conversions at the shallowest and deepest phase changes—such as seen between 30 and 43°N near the 660 in Figure 5a—could therefore also be used to infer mantle composition.

In a subsequent paper, we will investigate in more detail whether the complexity in the MTZ imaged by *P*-to-*S* RFs and SS precursors beneath northeast Asia can be explained solely by solid state phase equilibria in a subduction-dominated environment or whether other factors (e.g., melting) are necessary.

5. Conclusion

We used two independent approaches of teleseismic imaging, *P*-to-*S* RFs and SS precursors, to provide new seismic constraints on the MTZ structure below northeast Asia. We found significant complexity, both in terms of the topography of interfaces and of anomalous signals within and above the MTZ. In particular, from RFs, we confirmed an apparent doubling of the 660-km discontinuity over a 890×350 km^2 region between 36–44°N and 130–133°E at the tip of the subducted Pacific plate. Due to resolution limitations, this zone cannot be detected with SS precursors. We found a similar level of complexity on the 410-km discontinuity, coinciding with the presence of a deep cluster of seismicity below the Japan Sea. Both methods suggest the presence of low-velocity zones surrounding MTZ mineralogical phase changes. We discussed the observed seismic waveforms in light of a phase diagram for a pyrolitic model of mantle composition and thermal models of the MTZ. Instead of manifesting as simple first-order discontinuities, solid-solid phase transitions result in broad zones of velocity gradients with some local and marked discontinuities associated with the main transitions in olivine, pyroxenes and garnet. The variability in seismic properties predicted by phase equilibria computations can account for much of the complexity observed beneath northeast Asia. In particular, the stability of stishovite at high pressures (23–30 GPa) and low temperatures (< 1200 K) can explain the low-velocity zones and anomalous reflectivities observed in this region above and below the 660-km discontinuity. This interpretation has broader implications for the interpretation of seismic observations in other cold MTZ settings around the world.

Acknowledgments
The global traveltime measurements of waves converted from *P*-to-*S* at MTZ discontinuities are available from B. T. personal webpage http://perso.ens-lyon.fr/benoit.tauzin/TransitionZone.htm. The facilities from the IRIS Data Management Center, the Korea Institute of Geosciences and Mineral Resources, the Korean Meteorological Administration, and the NIED were used for access to waveforms and related metadata used in this study. IRIS Data Services are funded through the Seismological Facilities for the Advancement of Geoscience and EarthScope (SAGE) Proposal of the National Science Foundation under Cooperative Agreement EAR-1261681. When available, the DOIs for permanent and temporary networks used in this study have been listed in the references. The data from Korea can be obtained in part through direct request from the Korea Institute of Geoscience and Mineral Resources (KIGAM; http://english.kigam.re.kr/html/en/) and Korean Meteorological Administration (KMA; https://web.kma.go.kr/eng/weather/kma_service/cooperation.jsp), and in part from IRIS (http://www.iris.washington.edu/mda/KG and http://www.iris.washington.edu/mda/KS). Direct sharing of the processed data is possible through personal e-mail request. B. T. was supported by a delegation from the French Centre National de la Recherche Scientifique (CNRS) and a Congé pour Recherche et Conversion Thématique from the Université Claude Bernard Lyon 1 (UCBL), to visit the Research School in Earth Sciences (RSES) at the Australian National University (ANU). S. K. was funded by the Korea Meteorological Administration under grant KMI2017-01010. The work of J. C. A. was supported by an ARC DP project (DP160103502) and Macquarie University grants. We thank Lars Stixrude and Ian Jackson for valuable discussions on possible MTZ stability fields. We thank A. M. Negredo for making available TEMSPOL. This is contribution 1157 from the ARC Centre of Excellence for Core to Crust Fluid Systems (http://www.ccfs.mq.edu.au) and 1223 in the GEMOC Key Centre (http://www.gemoc.mq.edu.au).

References

Albuquerque Seismological Laboratory (ASL)/USGS (1986). China Digital Seismograph Network. International Federation of Digital Seismograph Networks. Other/Seismic Network. https://doi.org/10.7914/SN/CD

Albuquerque Seismological Laboratory (ASL)/USGS (1988). Global Seismograph Network (GSN - IRIS/USGS). International Federation of Digital Seismograph Networks. Other/Seismic Network. https://doi.org/10.7914/SN/IU

Albuquerque Seismological Laboratory (ASL)/USGS (1990). United States National Seismic Network. International Federation of Digital Seismograph Networks. Other/Seismic Network. https://doi.org/10.7914/SN/US

Albuquerque Seismological Laboratory (ASL)/USGS (1993). Global Telemetered Seismograph Network (USAF/USGS). International Federation of Digital Seismograph Networks. Other/Seismic Network. https://doi.org/10.7914/SN/GT

Ai, Y., & Zheng, T. (2003). The upper mantle discontinuity structure beneath eastern China. *Geophysical Research Letters*, *21*, 2089.

Ammon, C. (1991). The isolation of receiver effects from teleseismic P waveforms. *Bulletin of the Seismological Society of America*, *81*, 2504–2510.

Baker, M. B., & Stolper, E. M. (1994). Determining the composition of high-pressure mantle melts using diamond aggregates. *Geochimica et Cosmochimica Acta*, *58*(13), 2811–2827.

Bercovici, D., & Karato, S. (2003). Whole mantle convection and transition-zone water filter. *Nature*, *425*, 39–44.

Bina, C., & Helffrich, G. (1994). Phase transition Clapeyron slopes and transition zone seismic discontinuity topography. *Journal of Geophysical Research*, *99*(B8), 15,853–15,860.

Bonatto, L., Schimmel, M., Gallart, J., & Morales, J. (2015). The upper-mantle transition zone beneath the Ibero-Maghrebian region as seen by teleseismic Pds phases. *Tectonophysics*, *663*, 212–224.

Chaljub, E., & Tarantola, A. (1997). Sensitivity of SS precursors to topography on the upper-mantle 660-km discontinuity. *Geophysical Research Letters*, *24*(21), 2613–2616.

Chambers, K., Woodhouse, J., & Deuss, A. (2005). Topography of the 410-km discontinuity from PP and SS precursors. *Earth and Planetary Science Letters*, *235*, 610–622.
Cheng, C., Bodin, T., Tauzin, B., & Allen, R. M. (2017). Cascadia subduction slab heterogeneity revealed by three-dimensional receiver function Kirchhoff migration. *Geophysical Research Letters*, *44*, 694–701. https://doi.org/10.1002/2016GL072142
Chevrot, S., Vinnik, L., & Montagner, J. (1999). Global-scale analysis of the mantle Pds phases. *Journal of Geophysical Research*, *101*(B9), 20,203–20,219.
Choy, G. L., & Richards, P. G. (1975). Pulse distortion and Hilbert transformation in multiple reflected and refracted body waves. *Bulletin of the Seismological Society of America*, *65*(1), 55–70.
Connolly, J. (2009). The geodynamic equation of state: What and how. *Geochemistry, Geophysics, Geosystems*, *10*, Q10014. https://doi.org/10.1029/2009GC002540
Cottaar, S., & Deuss, A. (2016). Large-scale mantle discontinuity topography beneath Europe: Signature of akimotoite in subducting slabs. *Journal of Geophysical Research: Solid Earth*, *121*, 279–292. https://doi.org/10.1002/2015JB012452
Dahlen, F. (2005). Finite-frequency sensitivity kernels for boundary topography perturbations. *Geophysical Journal International*, *162*, 525–540.
Debayle, E., Dubuffet, F., & Durand, S. (2016). An automatically updated S-wave model of the upper mantle and the depth extent of azimuthal anisotropy. *Geophysical Research Letters*, *43*, 674–682. https://doi.org/10.1002/2015GL067329
Deuss, A. (2009). Global observations of mantle discontinuities using SS and PP precursors. *Surveys in Geophysics*, *30*(4-5), 301–326.
Deuss, A., Andrews, J., & Day, E. (2013). Seismic observations of mantle discontinuities and their mineralogical and dynamical interpretation. In S.-I. Karato (Ed.), *Physics and Chemistry of the Deep Earth* (pp. 297–323). Chichester, UK: John Wiley.
Deuss, A., Redfern, S., Chambers, K., & Woodhouse, J. (2006). The nature of the 660-Kilometer discontinuity in Earth's mantle from global seismic observations of pp precursors. *Science*, *311*, 198–201.
Dokht, R. M., Gu, Y. J., & Sacchi, M. D. (2016). Waveform inversion of SS precursors: An investigation of the northwestern pacific subduction zones and intraplate volcanoes in china. *Gondwana Research*, *40*, 77–90.
Eager, K., Fouch, M., & James, D. (2010). Receiver function imaging of upper mantle complexity beneath the Pacific Northwest, United States. *Earth and Planetary Science Letters*, *297*, 140–152.
Efron, B., & Tibshirani, R. (1991). Statistical Data Analysis in the Computer Age. *Science*, *253*, 390–395.
Faccenda, M., & Dal Zilio, L. (2017). The role of solid-solid phase transitions in mantle convection. *Lithos*, *268*, 198–224.
Flanagan, M. P., & Shearer, P. M. (1998). Global mapping of topography on transition zone velocity discontinuities by stacking SS precursors. *Journal of Geophysical Research*, *103*(B2), 2673–2692.
Fuchs, K., & Muller, G. (1971). Computation of synthetic seismograms with the reflectivity method and comparison with observations. *Geophysical Journal International*, *23*, 417–433.
Gao, Y., Suetsugu, D., Fukao, Y., Obayashi, M., Shi, Y., & Liu, R. (2010). Seismic discontinuities in the mantle transition zone and at the top of the lower mantle beneath eastern China and Korea: Influence of the stagnant Pacific slab. *Physics of the Earth and Planetary Interiors*, *183*(1), 288–295.
GEOFON Data Centre (1993). GEOFON Seismic Network. Deutsches GeoForschungsZentrum GFZ. Other/Seismic Network. https://doi.org/10.14470/TR560404
Geological Survey of Canada (1989). Canadian National Seismograph Network. International Federation of Digital Seismograph Networks. Other/Seismic Network. https://doi.org/10.7914/SN/CN
GEOSCOPE (1982). French Global Network of Broad Band Seismic Stations. Institut de Physique du Globe de Paris (IPGP). https://doi.org/10.18715/GEOSCOPE.G
Gu, Y., Dziewonski, A., & Agee, C. (1998). Global de-correlation of the topography of transition zone discontinuities. *Earth and Planetary Science Letters*, *157*, 57–67.
Gu, Y. J., Okeler, A., & Schultz, R. (2012). Tracking slabs beneath northwestern Pacific subduction zones. *Earth and Planetary Science Letters*, *331*, 269–280.
Hayes, G. P., Wald, D. J., & Johnson, R. L. (2012). Slab1. 0: A three-dimensional model of global subduction zone geometries. *Journal of Geophysical Research*, *117*, B01302. https://doi.org/10.1029/2011JB008524
Hier-Majumder, S., & Tauzin, B. (2017). Pervasive upper mantle melting beneath the western US. *Earth and Planetary Science Letters*, *463*, 25–35.
Hirose, K. (2002). Phase transitions in pyrolitic mantle around 670-km depth: Implications for upwelling of plumes from the lower mantle. *Journal of Geophysical Research*, *107*(B4), 107.
Houser, C., Masters, G., Flanagan, M., & Shearer, P. (2008). Determination and analysis of long-wavelength transition zone structure using SS precursors. *Geophysical Journal International*, *174*, 178–194.
Houser, C., Masters, G., Shearer, P., & Laske, G. (2008). Shear and compressional velocity models of the mantle from cluster analysis of long-period waveforms. *Geophysical Journal International*, *174*(1), 195–212.
Huang, J., & Zhao, D. (2006). High-resolution mantle tomography of China and surrounding regions. *Journal of Geophysical Research*, *111*, B09305. https://doi.org/10.1029/2005JB004066
Kennett, B., & Engdahl, E. (1991). Travel times for global earthquake location and phase identification. *Geophysical Journal International*, *105*, 429–465.
Koroni, M., Bozdağ, E., Paulssen, H., & Trampert, J. (2017). Sensitivity analysis of seismic waveforms to upper-mantle discontinuities using the adjoint method. *Geophysical Journal International*, *210*(3), 1965–1980.
Koroni, M., & Trampert, J. (2015). The effect of topography of upper-mantle discontinuities on SS precursors. *Geophysical Journal International*, *204*(1), 667–681.
Lawrence, J., & Shearer, P. (2006). A global study of transition zone thickness using receiver functions. *Journal of Geophysical Research*, *111*, B06307. https://doi.org/10.1029/2005JB003973
Lawrence, J. F., & Shearer, P. M. (2008). Imaging mantle transition zone thickness with SdS-SS finite-frequency sensitivity kernels. *Geophysical Journal International*, *174*, 143–158. https://doi.org/10.1111/j.1365-246X.2007.03673.x
Lee, S.-H., Rhie, J., Park, Y., & Kim, K.-H. (2014). Topography of the 410 and 660 km discontinuities beneath the Korean Peninsula and southwestern Japan using teleseismic receiver functions. *Journal of Geophysical Research: Solid Earth*, *119*, 7245–7257. https://doi.org/10.1002/2014JB011149
Li, X., Sobolev, S., Kind, R., Yuan, X., & Estabrook, C. (2000). A detailed receiver function image of the upper mantle discontinuities in the Japan subduction zone. *Earth and Planetary Science Letters*, *183*, 527–541.
Li, C., & Van Der Hilst, R. D. (2010). Structure of the upper mantle and transition zone beneath Southeast Asia from traveltime tomography. *Journal of Geophysical Research*, *115*, B07308. https://doi.org/10.1029/2009JB006882

Ligorrìa, J., & Ammon, C. (1999). Iterative deconvolution and receiver-function estimation. *Bulletin of the Seismological Society of America*, *85*, 1395–1400.
Liu, Z., Niu, F., Chen, Y. J., Grand, S., Kawakatsu, H., Ning, J., et al. (2015). Receiver function images of the mantle transition zone beneath ne China: New constraints on intraplate volcanism, deep subduction and their potential link. *Earth and Planetary Science Letters*, *412*, 101–111.
Liu, Z., Park, J., & Karato, S.-i. (2016). Seismological detection of low-velocity anomalies surrounding the mantle transition zone in Japan subduction zone. *Geophysical Research Letters*, *43*, 2480–2487. https://doi.org/10.1002/2015GL067097
Liu, X., Zhao, D., Li, S., & Wei, W. (2017). Age of the subducting pacific slab beneath East Asia and its geodynamic implications. *Earth and Planetary Science Letters*, *464*, 166–174.
Millet, F., Bodin, T., & Rondenay, S. (2017). Towards 3D Kirchhoff migration of receiver functions at continental scale, IAG-IASPEI.
Monteiller, V., Chevrot, S., Komatitsch, D., & Fuji, N. (2012). A hybrid method to compute short-period synthetic seismograms of teleseismic body waves in a 3-d regional model. *Geophysical Journal International*, *192*, 230–247. https://doi.org/10.1093/gji/ggs006
Müller, R. D., Sdrolias, M., Gaina, C., & Roest, W. R. (2008). Age, spreading rates, and spreading asymmetry of the world's ocean crust. *Geochemistry, Geophysics, Geosystems*, *9*, Q04006. https://doi.org/10.1029/2007GC001743
Negredo, A., Valera, J., & Carminati, E. (2004). TEMSPOL: A MATLAB thermal model for deep subduction zones including major phase transformations. *Computers & Geosciences*, *30*(3), 249–258.
Niu, F. (2014). Distinct compositional thin layers at mid-mantle depths beneath northeast China revealed by the USArray. *Earth and Planetary Science Letters*, *402*, 305–312.
Niu, F., & Kawakatsu, H. (1996). Complex structure of mantle discontinuities at the tip of the subducting slab beneath north-east China. *Journal of Physics of the Earth*, *44*, 701–711.
Niu, F., Levander, A., Ham, S., & Obayashi, M. (2005). Mapping the subducting Pacific slab beneath southwest Japan with Hi-net receiver functions. *Earth and Planetary Science Letters*, *239*, 9–17.
Obayashi, M., Yoshimitsu, J., Nolet, G., Fukao, Y., Shiobara, H., Sugioka, H., et al. (2013). Finite frequency whole mantle p wave tomography: Improvement of subducted slab images. *Geophysical Research Letters*, *40*, 5652–5657. https://doi.org/10.1002/2013GL057401
Press, W., Flannery, B., Teukolsky, S., & Vetterling, W. (1992). *Numerical recipes in C: The art of scientific computing*. Cambridge: Cambridge University Press.
Sambridge, M., & Faletič, R. (2003). Adaptive whole Earth tomography. *Geochemistry, Geophysics, Geosystems*, *4*(3), 1022. https://doi.org/10.1029/2001GC000213
Schmandt, B., Dueker, K., Humphreys, E., & Hansen, S. (2012). Hot mantle upwelling across the 660 beneath Yellowstone. *Earth and Planetary Science Letters*, *331-332*, 224–236.
Schmandt, B., Jacobsen, S. D., Becker, T. W., Liu, Z., & Dueker, K. G. (2014). Dehydration melting at the top of the lower mantle. *Science*, *344*(6189), 1265–1268.
Schmerr, N. (2012). The gutenberg discontinuity: Melt at the lithosphere-asthenosphere boundary. *Science*, *335*(6075), 1480–1483.
Schmerr, N., & Garnero, E. (2006). Investigation of upper mantle discontinuity structure beneath the central pacific using SS precursors. *Journal of Geophysical Research*, *111*, B08305. https://doi.org/10.1029/2005JB004197
Schmerr, N., & Garnero, E. (2007). Upper mantle discontinuity topography from thermal and chemical heterogeneity. *Science*, *318*, 623–626.
Schmerr, N. C., Kelly, B. M., & Thorne, M. S. (2013). Broadband array observations of the 300 km seismic discontinuity. *Geophysical Research Letters*, *40*, 841–846. https://doi.org/10.1002/grl.50257
Scripps Institution of Oceanography (1986). IRIS/IDA Seismic Network. International Federation of Digital Seismograph Networks. Other/Seismic Network. https://doi.org/10.7914/SN/II
Shearer, P. (1991). Constraints on upper mantle discontinuities from observations of long-period reflected and converted phases. *Journal of Geophysical Research*, *96*(B11), 18,147–18,182.
Shearer, P. (1996). Transition zone velocity gradients and the 520-km discontinuity. *Journal of Geophysical Research*, *101*(B2), 3053–3066.
Shearer, P., Flanagan, M., & Hedlin, M. (1999). Experiments in migration processing of SS precursor data to image upper mantle discontinuity structure. *Journal of Geophysical Research*, *104*(B4), 7229–7242.
Shen, Y., & Blum, J. (2003). Seismic evidence for accumulated oceanic crust above the 660-km discontinuity beneath southern Africa. *Geophysical Research Letters*, *30*(18), 1925.
Shen, X., Yuan, X., & Li, X. (2014). A ubiquitous low-velocity layer at the base of the mantle transition zone. *Geophysical Research Letters*, *41*, 836–842. https://doi.org/10.1002/2013GL058918
Shen, X., Zhou, H., & Kawakatsu, H. (2008). Mapping the upper mantle discontinuities beneath China with teleseismic receiver functions. *Earth, Planets and Space*, *60*, 713–719.
Sigloch, K., & Nolet, G. (2006). Measuring finite-frequency body-wave amplitudes and traveltimes. *Geophysical Journal International*, *167*, 271–287. https://doi.org/10.1111/j.1365-246X.2006.03116.x
Simmons, N. A., & Gurrola, H. (2000). Multiple seismic discontinuities near the base of the transition zone in the Earth's mantle. *Nature*, *405*, 559–562.
Stixrude, L., & Lithgow-Bertelloni, C. (2005). Mineralogy and elasticity of the oceanic upper mantle: Origin of the low-velocity zone. *Journal of Geophysical Research*, *110*, B03204. https://doi.org/10.1029/2004JB002965
Stixrude, L., & Lithgow-Bertelloni, C. (2011). Thermodynamics of mantle minerals—II. Phase equilibria. *Geophysical Journal International*, *184*, 1180–1213. https://doi.org/10.1111/j.1365-246X.2010.04890.x
Syracuse, E. M., van Keken, P. E., & Abers, G. A. (2010). The global range of subduction zone thermal models. *Physics of the Earth and Planetary Interiors*, *183*(1), 73–90.
Tang, Y., Obayashi, M., Niu, F., Grand, S. P., Chen, Y. J., Kawakatsu, H., et al. (2014). Changbaishan volcanism in northeast China linked to subduction-induced mantle upwelling. *Nature Geoscience*, *7*(6), 470–475.
Tauzin, B., Afonso, J.-C., Sambridge, M., Tkalcic, H., Kim, S., & Bodin, T. (2017). Towards a fully probabilistic reconstruction of the elastic, thermal and petrological structure of the Earth's mantle transition zone (pp. 5855).
Tauzin, B., Debayle, E., & Wittlinger, G. (2008). The mantle transition zone as seen by global Pds phases: No clear evidence for a thin transition zone beneath hotspots. *Journal of Geophysical Research*, *113*, B08309. https://doi.org/10.1029/2007JB005364
Tauzin, B., Debayle, E., & Wittlinger, G. (2010). Seismic evidence for a global low velocity layer within the Earth's upper mantle. *Nature Geoscience*, *3*, 718–721.
Tauzin, B., Kim, S., & Kennett, B. (2017). Pervasive seismic low-velocity zones within stagnant plates in the mantle transition zone: Thermal or compositional origin? *Earth and Planetary Science Letters*, *477*, 1–13.

Tauzin, B., & Ricard, Y. (2014). Seismically deduced thermodynamics phase diagrams for the mantle transition zone. *Earth and Planetary Science Letters*, *401*, 337–346.

Tauzin, B., van der Hilst, R., Wittlinger, G., & Ricard, Y. (2013). Multiple transition zone seismic discontinuities and low velocity layers below western United States. *Journal of Geophysical Research*, *118*, 2307–2322. https://doi.org/10.1002/jgrb.50182

Tian, Y., Zhu, H., Zhao, D., Liu, C., Feng, X., Liu, T., & Ma, J. (2016). Mantle transition zone structure beneath the Changbai volcano: Insight into deep slab dehydration and hot upwelling near the 410 km discontinuity. *Journal of Geophysical Research: Solid Earth*, *121*, 5794–5808. https://doi.org/10.1002/2016JB012959

Vacher, P., Mocquet, A., & Sotin, C. (1998). Computation of seismic profiles from mineral physics: The importance of the non-olivine components for explaining the 660 km depth discontinuity. *Physics of the Earth and Planetary Interiors*, *106*, 275–298.

Vinnik, L., & Farra, V. (2007). Low velocity atop the 410-km discontinuity and mantle plumes. *Earth and Planetary Science Letters*, *262*, 398–412.

Wang, Z., & Dahlen, F. (1995). Spherical-spline parameterization of three-dimensional Earth models. *Geophysical Research Letters*, *22*(22), 3099–3102.

Wei, S. S., & Shearer, P. M. (2017). A sporadic low-velocity layer atop the 410-km discontinuity beneath the Pacific Ocean. *Journal of Geophysical Research: Solid Earth*, *122*, 5144–5159. https://doi.org/10.1002/2017JB014100

Weidner, D., & Wang, Y. (1998). Chemical- and Clapeyron-induced buoyancy at the 660 km discontinuity. *Journal of Geophysical Research*, *103*(B4), 7431–7441.

Wittlinger, G., Vergne, J., Tapponnier, P., Farra, V., Poupinet, G., Jiang, M., et al. (2004). Teleseismic imaging of subducting lithosphere and Moho offsets beneath western Tibet. *Earth and Planetary Science Letters*, *221*, 117–130.

Yang, T., Moresi, L., Zhao, D., Sandiford, D., & Whittaker, J. (2018). Cenozoic lithospheric deformation in northeast Asia and the rapidly-aging Pacific plate. *Earth and Planetary Science Letters*, *492*, 1–11.

Zhang, Z., Dueker, K. G., & Huang, H. H. (2018). Ps mantle transition zone imaging beneath the Colorado Rocky Mountains: Evidence for an upwelling hydrous mantle. *Earth and Planetary Science Letters*, *492*, 197–205.

Zhao, L., & Chevrot, S. (2003). SS-wave sensitivity to upper mantle structure: Implications for the mapping of transition zone discontinuity topographies. *Geophysical Research Letters*, *30*(11), 1590.

Zunino, A., Khan, A., Cupillard, P., & Mosegaard, K. (2016). Constitution and structure of Earth's mantle: Insights from mineral physics and seismology. *Integrated Imaging of the Earth: Theory and Applications*, *218*, 219.